Using U-Th-Pb petrochronology to determine rates of ductile thrusting: time windows into the Main Central Thrust, Sikkim Himalaya

AGU PUBLICATIONS

Tectonics

RESEARCH ARTICLE
10.1002/2014TC003743

Key Points:
- Petrochronology tools used to link monazite age to metamorphic stage
- Time windows into ductile thrusting history of Himalayan structure revealed
- Novel technique indicates that thrusting occurred at a minimum rate of ~10 ± 3 mm yr^{-1}

Supporting Information:
- Supporting Information S1: Texts S1–S11, Figures S1–S9, and Tables S1–S10
- Data Set S1
- Data Set S2
- Data Set S3

Correspondence to:
C. M. Mottram,
c.m.mottram@googlemail.com

Citation:
Mottram, C. M., R. R. Parrish, D. Regis, C. J. Warren, T. W. Argles, N. B. W. Harris, and N. M. W. Roberts (2015), Using U-Th-Pb petrochronology to determine rates of ductile thrusting: Time windows into the Main Central Thrust, Sikkim Himalaya, *Tectonics*, *34*, doi:10.1002/2014TC003743.

Received 22 SEP 2014
Accepted 21 MAY 2015
Accepted article online 26 MAY 2015

Using U-Th-Pb petrochronology to determine rates of ductile thrusting: Time windows into the Main Central Thrust, Sikkim Himalaya

Catherine M. Mottram[1,2], Randall R. Parrish[3,4], Daniele Regis[1], Clare J. Warren[1], Tom W. Argles[1], Nigel B. W. Harris[1], and Nick M. W. Roberts[4]

[1]Department of Environment, Earth and Ecosystems, Open University, Milton Keynes, UK, [2]Department of Earth Science, University of California, Santa Barbara, California, USA, [3]Department of Geology, University of Leicester, Leicester, UK, [4]NERC Isotope Geosciences Laboratory, British Geological Survey, Nottingham, UK

Abstract Quantitative constraints on the rates of tectonic processes underpin our understanding of the mechanisms that form mountains. In the Sikkim Himalaya, late structural doming has revealed time-transgressive evidence of metamorphism and thrusting that permit calculation of the minimum rate of movement on a major ductile fault zone, the Main Central Thrust (MCT), by a novel methodology. U-Th-Pb monazite ages, compositions, and metamorphic pressure-temperature determinations from rocks directly beneath the MCT reveal that samples from ~50 km along the transport direction of the thrust experienced similar prograde, peak, and retrograde metamorphic conditions at different times. In the southern, frontal edge of the thrust zone, the rocks were buried to conditions of ~550°C and 0.8 GPa between ~21 and 18 Ma along the prograde path. Peak metamorphic conditions of ~650°C and 0.8–1.0 GPa were subsequently reached as this footwall material was underplated to the hanging wall at ~17–14 Ma. This same process occurred at analogous metamorphic conditions between ~18–16 Ma and 14.5–13 Ma in the midsection of the thrust zone and between ~13 Ma and 12 Ma in the northern, rear edge of the thrust zone. Northward younging muscovite $^{40}Ar/^{39}Ar$ ages are consistently ~4 Ma younger than the youngest monazite ages for equivalent samples. By combining the geochronological data with the >50 km minimum distance separating samples along the transport axis, a minimum average thrusting rate of 10 ± 3 mm yr^{-1} can be calculated. This provides a minimum constraint on the amount of Miocene India-Asia convergence that was accommodated along the MCT.

1. Introduction

Current rates of relative displacement within the crust in modern orogens can be precisely quantified using geodetic and geophysical data [*Banerjee and Bürgmann*, 2002; *Bettinelli et al.*, 2006; *Bilham et al.*, 1997; *Larson et al.*, 1999]. However, these data cannot readily be extrapolated back in time to determine whether earlier movement was accommodated at the same rate. This is partially due to the episodic nature of recent abrupt seismic events that contrast markedly with the long-term effect of distributed ductile strain through geological time. Empirical evidence from preserved shear zones provides the opportunity for determining how convergence has been accommodated along different structures in the past. Key to this determination is the accurate and precise linking of the pressure-temperature (P-T) conditions of crystallization of accessory minerals that record time (such as monazite or zircon) to the P-T conditions recorded by major phases (such as garnet) during the thrusting process.

Since the mid-Miocene (~34 Ma) slowdown in convergence, which lasted until ~10 Ma [*Iaffaldano et al.*, 2013], India and Asia have been converging at ~83–55 mm yr^{-1} [*Copley et al.*, 2010; *Molnar and Stock*, 2009; *van Hinsbergen et al.*, 2011], ~20 mm yr^{-1} of which is thought to have been accommodated by deformation within the Himalayan orogen south of the Indus-Tsangpo suture. Current convergence is taken up by a combination of lithospheric thickening of the Tibetan Plateau [*Bettinelli et al.*, 2006; *Bilham et al.*, 1997; *Burgess et al.*, 2012; *Larson et al.*, 1999; *Lavé and Avouac*, 2001] and tectonic escape along the eastern boundary [*Clark and Bilham*, 2008], in addition to that within the Himalaya. The majority of the latter is thought to be accommodated by displacement along the Main Himalayan Thrust (MHT) [*Bilham et al.*, 1997; *Larson et al.*, 1999]. The locus of the ~150–200 km of shortening in the

frontal Himalaya [*Long et al.*, 2011; *Mitra et al.*, 2010] was accommodated in the past by more hinterland-located MHT-parallel thrusts, such as the Main Central Thrust (MCT), with overall deformation propagating toward the foreland as collision progressed [*Robinson and McQuarrie*, 2012; *Robinson and Pearson*, 2013].

Rates of past movement on these major faults can be inferred by considering the duration of deformation from geochronological or stratigraphic data and by estimating the amount of displacement accommodated along them. These latter estimates are often imprecise, since large displacements and pervasive deformation commonly preclude the matching of hanging wall and footwall marker horizons.

Previous estimates of Himalayan shortening rates have largely been based on distances estimated from either balanced cross sections [*McQuarrie et al.*, 2014; *Tobgay et al.*, 2012], the southward propagation of foreland basins [*Avouac*, 2003; *Lavé and Avouac*, 2000], or by modeled exhumation rates [*Avouac*, 2003; *Bollinger et al.*, 2004, 2006; *Herman et al.*, 2010]. While these methods can provide some constraint on the rate of near-surface fault displacement, none of them are applicable to the estimation of rates of deformation in the ductile regime, at midcrustal depths. Previous attempts to calculate the rate of ductile thrusting along the MCT in the Himalaya have relied strongly on thermal modeling for the estimation of the transport distance [*Corrie and Kohn*, 2011; *Kohn et al.*, 2004]. The large uncertainties associated with the temperature and time estimates are therefore propagated through to the rates calculation. To improve on this approach we use a more specific new method.

Our approach links the timing of crystallization of U-Th-Pb-bearing monazite (Ce phosphate) to the crystallization history of the main rock matrix [*Janots et al.*, 2008, 2009]. Trace-element "fingerprints" of monazite crystallization reactions recorded in major phases such as garnet allow mineral growth to be linked to P-T conditions. This is achieved through a combination of detailed petrography, geochemical analysis of coexisting accessory and major phases, and U-Th-Pb geochronology using samples from appropriate locations [*Foster et al.*, 2000, 2002, 2004; *Gasser et al.*, 2012; *Hermann and Rubatto*, 2003; *Hoisch et al.*, 2008; *Janots et al.*, 2006, 2007, 2008, 2009; *Kingsbury et al.*, 1993; *Kylander-Clark et al.*, 2013; *Mottram et al.*, 2014b; *Pyle and Spear*, 2003; *Rubatto et al.*, 2006; *Smith and Barreiro*, 1990; *Spear*, 2010; *Wing et al.*, 2003]. We have developed and applied these petrochronological techniques to reveal that samples at various distances across the strike of the Himalayan orogen progressively record similar P-T paths but at different times. We exploit the folded exposure of a major Himalayan ductile fault zone, the MCT, to estimate the minimum average rate of thrusting on this important structure.

2. Geological Setting

The West Bengali Darjeeling Hills and Sikkim regions of the eastern Himalaya (herein collectively described as the Sikkim Himalaya; Figure 1) provide an exceptional exposure of the MCT. The MCT crops out as an up to ~5–10 km thick zone of ductile shear, with an associated coevally developed zone of inverted Barrovian metamorphism in the footwall [*Anczkiewicz et al.*, 2014; *Catlos et al.*, 2004; *Dasgupta et al.*, 2004, 2009; *Gaidies et al.*, 2015]. Deformation propagated structurally downward during thrusting, promoting progressive accretion of slivers of footwall material to the hanging wall, and developing an inverted metamorphic sequence [*Mottram et al.*, 2014b].

In the Sikkim Himalaya, a late duplex (the Lesser Himalayan Duplex (LHD)) in the Lesser Himalayan Sequence (LHS) footwall rocks, folded the MCT and overlying Greater Himalayan Sequence (GHS) into the Teesta dome [*Bhattacharyya and Mitra*, 2009]. Subsequent erosion, centered on the Teesta River, has exposed different structural depths of the MCT, which crops out at the surface as one of the largest reentrants in the Himalaya (Figure 1a).

Six pelitic schist samples for U-Th-Pb analysis and three further schist samples for $^{40}Ar/^{39}Ar$ dating were collected from very similar structural levels of the upper LHS rocks within the ductile MCT shear zone, around the flanks of the dome (Figure 1 and Table S2 in the supporting information). These samples are pervasively sheared, display strong penetrative fabrics, and N-S directed stretching lineations, related to south directed thrusting along the MCT [*Dasgupta et al.*, 2004; *Goswami*, 2005; *Mottram et al.*, 2014a].

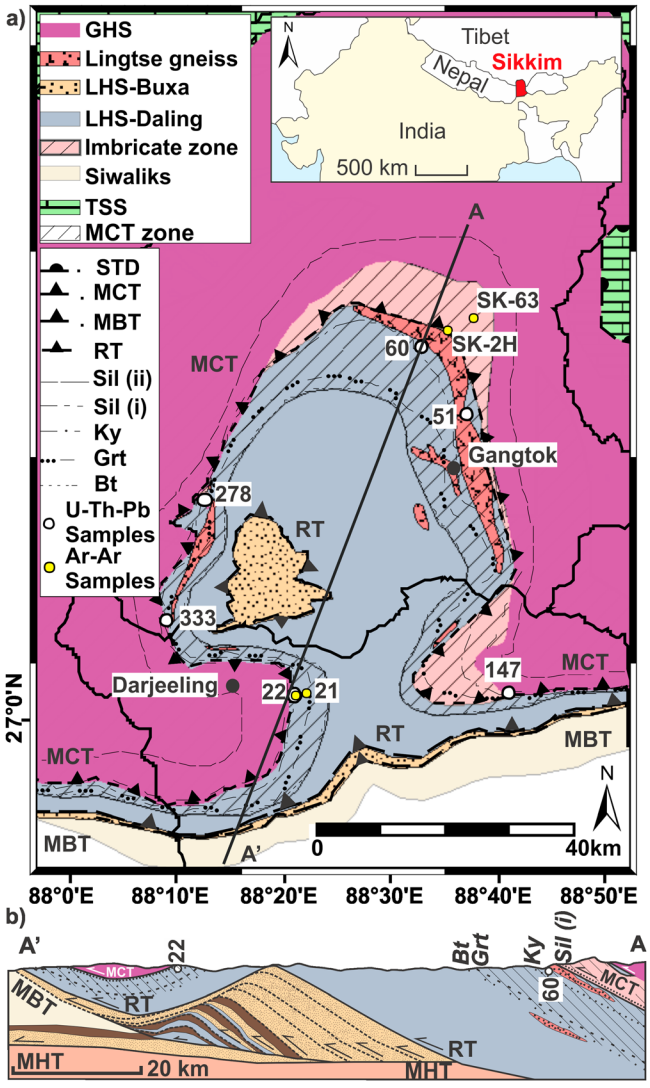

Figure 1. (a) Geological map and (b) cross section of the Sikkim Himalaya, adapted from *Mottram et al.* [2014a]. STD = South Tibetan Detachment, MCT = Main Central Thrust, RT = Ramgarh Thrust, MBT = Main Boundary Thrust, and MHT = Main Himalayan Thrust. Isograds: Sil (ii) = sillimanite (no muscovite), Sil (i) = fibrolite, Ky = kyanite, Gt = garnet, and Bt = biotite. GHS = Greater Himalayan Sequence, LG = Lingtse Gneiss (LHS), LHS = Lesser Himalayan Sequence, B = Buxa, D = Daling, IZ = Imbricate zone, SW = Siwaliks, and TSS = Tethyan Sedimentary Sequence. U-Th-Pb sample locations are shown in white circles, and $^{40}Ar/^{39}Ar$ sample locations are shown in yellow circles. LHS Duplex from *Bhattacharyya and Mitra* [2009].

3. Methods

3.1. Electron Microprobe Analysis (EPMA) and Scanning Electron Microscope (SEM)

Quantitative major element data and elemental X-ray maps were collected from polished thin section using the Open University Cameca SX100 EPMA and the Open University FEI Quanta 3-D dual beam microscope SEM. Full operating conditions are detailed in Texts S1.1 and S1.2 in the supporting information.

3.2. Pressure-Temperature Calculations and Modeling

Estimates of P-T conditions were calculated using the garnet-Al_2SiO_5-plagioclase thermobarometer of *Holdaway* [2000], the garnet-biotite thermometer of *Bhattacharya et al.* [1992], and the Zr-in-rutile thermometer [*Tomkins et al.* [2007] calibration], calculated at $P = 0.9$ GPa (from previous pressure estimates on these rocks [*Mottram et al.*, 2014b]). The Ti-in-biotite (TiB) thermometer [*Henry et al.*, 2005] was also used to constrain the prograde thermal history, though only applied to biotite trapped as prograde inclusions within garnet cores. The precision on the original TiB calibration is estimated at ±12°C at high temperatures. Here a larger uncertainty (±50°C) was applied to account for biotite crystallization outside the 0.3–0.6 GPa calibration range of the thermometer [*Warren et al.*, 2014].

Pseudosections of samples 51 and 278 (pseudosections of samples 22 and 60 presented in *Mottram et al.* [2014b]) were constructed using Perple_X_6.6.8 [*Connolly*, 1990, 2009] using the internally consistent thermodynamic data set and equation of state for H_2O of *Holland and Powell* [2011] [*Mottram et al.*, 2014b] (Text S1.3 in the supporting information). Samples were modeled in the system MnNKCFMASTH under fluid-saturated ($aH_2O = 1$) conditions. The effective bulk composition of each sample was calculated either from an adapted XRF composition (Table S7.1 in supporting information sample 51) or from calculating of the proportion of each mineral phase in the sample from analysis of thin section X-ray maps using ImageJ software (Table S7.2, sample 278 in the supporting information) [*Schneider et al.*, 2012].

The P-T conditions were constrained by comparing calculated wt % oxide isopleths of garnet (CaO, FeO, and MgO) and plagioclase (CaO and Na_2O) on the pseudosection with observed compositions of those phases where present.

3.3. U-Th-Pb Monazite Geochronology

U-Th-Pb isotope concentrations in monazite were analyzed at the Natural Environment Research Council (NERC) Isotope Geosciences Laboratories, UK, using a Nu Attom single-collector sector-field inductively coupled plasma mass spectrometer (ICP-MS) (Nu instruments, Wrexham, UK) and New Wave Research UP193ss (193 nm) Nd:YAG laser ablation system. Monazite grains are typically zoned with respect to yttrium (Y) and thorium (Th). EMPA-generated maps were used to select suitable laser ablation analysis points; conditions of 15 μm spot size at 5 Hz and ~2.5 J/cm^{-2} fluence were used (Figure S8.3 in the supporting information). The instrumental configuration and measurement procedures follow previous methods [*Mottram et al.*, 2014b] (Text S1.4 in the supporting information).

Both U-Pb and Th-Pb decay schemes can be used to date monazite (Figures 6 and 7, Data Set S1, and Text S1.4 in the supporting information). Due to the acquisition protocol, the ^{232}Th/^{208}Pb ages are typically less precise than the ^{238}U/^{206}Pb ages [*Mottram et al.*, 2014b]. Monazite crystals contain both common Pb and excess ^{230}Th, which produce measured ages from both ^{206}U/^{238}Pb and ^{232}Th/^{208}Pb systems in excess of the crystallization age, and so cause data to diverge from concordia (Figure S9.1 in the supporting information). The data were corrected for both common Pb and excess ^{230}Th (using common Pb value of *Stacey and Kramers* [1975] and corrections outlined in Text S1.4 and Figure S1.4.1 in the supporting information]. For the majority of samples (60, 51, 147, and 22) there is close agreement between the (common Pb) corrected ^{238}U/^{206}Pb and ^{232}Th/^{208}Pb ages. However, for samples 278 and 333, there is some scatter. Because there is good reproducibility of standard material throughout the analyses (uncertainties between 1 and 4% (1σ); Text S1.4 in the supporting information), the most likely cause of the variance between the Th-Pb and U-Pb systems in these samples is due to the small grain size (generally ~20 μm; Figures S8.2.5 and S8.2.6 in the supporting information), which could have caused ablation pits to sample material across chemical zones and/or grain boundaries. Samples 278 and 333 both record systematic age-petrographic relationships, such that monazite included in garnet cores yields older ages than monazite included in the garnet rim or matrix. This suggests that the U-Pb ages are reliable. For internal consistency, we have quoted the weighted average common Pb and Th-corrected ^{206}Pb/^{238}U ages and uncertainties (±2σ) of monazite populations for all samples, as defined by either their petrological position or geochemical zoning patterns. For comparison, the Th-Pb data are also shown in both Figure 7 and in Figure S9 in the supporting information. The age uncertainties for each monazite population are shown for the weighted mean population age and include propagated systematic uncertainties for long-term variance, reference material age uncertainties, and decay constant uncertainty.

3.4. Trace Element Data

Monazite and garnet trace element and Zr-in-rutile concentrations were acquired at the Open University, UK, using a Agilent 7500 quadrupole ICP-MS coupled to a New Wave Research UP213 (213 nm) Nd:YAG laser ablation system [*Mottram et al.*, 2014b; Text S1.5 in the supporting information].

3.5. ^{40}Ar/^{39}Ar Methods

Single-grain fusion (sgf) analyses of muscovite were performed at the Open University, UK. Samples were crushed, washed, and sieved and ~20~0.5–1 mm diameter grains of the least deformed, most inclusion-free muscovite were picked from each sample (Figure S1.5 in the supporting information). Grains were washed in acetone and distilled water before packing into Al foil packets for irradiation.

All samples were irradiated at McMaster University in Canada. Irradiation flux was monitored using the GA1550 biotite standard with an age of 99.77 ± 0.11 Ma [*Renne et al.*, 2010]. J values were calculated by linear interpolation between two bracketing standards; a standard was included between every 8 and 10 samples in the irradiation tube (Text S1.6 in the supporting information).

Total fusion of single grains was achieved using a Nd-YAG 1064 nm infrared laser coupled to an automated gas handling vacuum system and admitted into a MAP 215–50 noble gas mass spectrometer.

Data were corrected using an in-house software package (ArMaDiLo) developed by J. Schwanethal and plotted using Isoplot [*Ludwig*, 2003]. Uncertainties on measurements are 1σ, and uncertainties on ages are 2σ and include the analytical, standard age, and decay constant uncertainties. The ^{40}K-^{40}Ar decay constant of *Min et al.* [2000] was used throughout. Full methods are recorded in Text S1.6 in the supporting information.

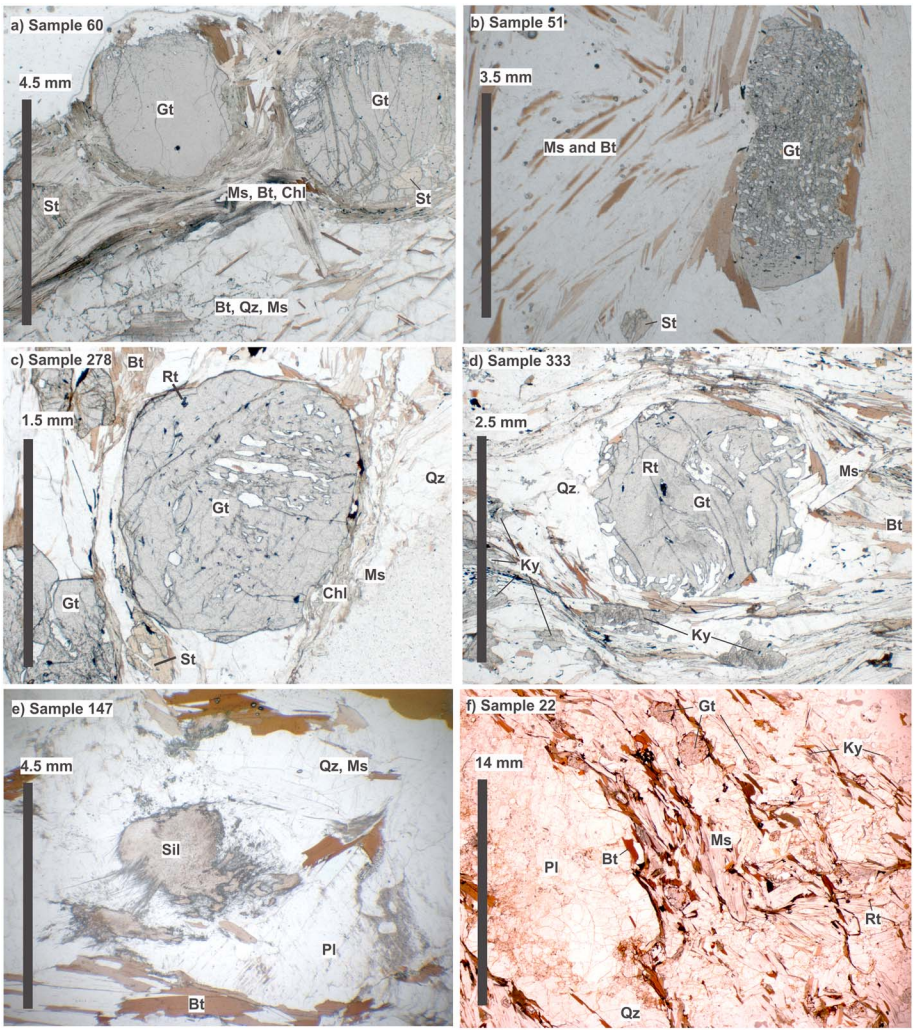

Figure 2. Thin section photomicrographs (all plane-polarized light, scale shown). (a) Sample 60, (b) sample 51, (c) sample 278, (d) sample 333, (e) sample 147, and (f) sample 22.

4. Results

4.1. Petrology/Mineral Chemistry

Six kyanite-bearing schist samples (60, 51, 278, 333, 147, and 22; Figure 2 and Tables S2–S3 and Figures S4–S5 in the supporting information) were collected from the footwall (LHS) of the MCT. Samples contain garnet + kyanite + quartz + muscovite + biotite ± staurolite (samples 60, 51, 278, 333, 147, and 22) ± plagioclase (samples 51, 147, and 22) ± fibrolitic sillimanite (samples 278, 147, and 22). Accessory phases include monazite + zircon + ilmenite ± apatite (samples 51, 278, 333, 147, and 22) ± rutile (samples 278, 333, and 22) ± tourmaline (samples 278, 333, and 22) ± xenotime (samples 147) ± allanite (sample 60). Some accessory phases are only present as inclusions within garnet (rutile in samples 60, 51, and 147; apatite in sample 60 and xenotime in sample 22). All samples preserve evidence for multiple stages of synkinematic mineral growth, including spiral inclusion trails within both garnet and kyanite (Figures 2 and 3) and with crystals aligned along the dominant penetrative foliation caused by south directed thrusting.

Garnet grains all have partially resorbed cores and differing major and trace element zoning patterns (Figure 3 and Figures S4–S5 in the supporting information). Garnet grains in sample 51 have inclusion-rich cores that preserve synkinematic inclusion trails and an average composition of $X_{Ca} = 0.07$, $X_{Mg} = 0.12$, $X_{Fe} = 0.79$, and $X_{Mn} = 0.03$. A later asymmetric Mn-depleted ($X_{Mn} = 0.01$) rim grew over the core. Both the core and rim

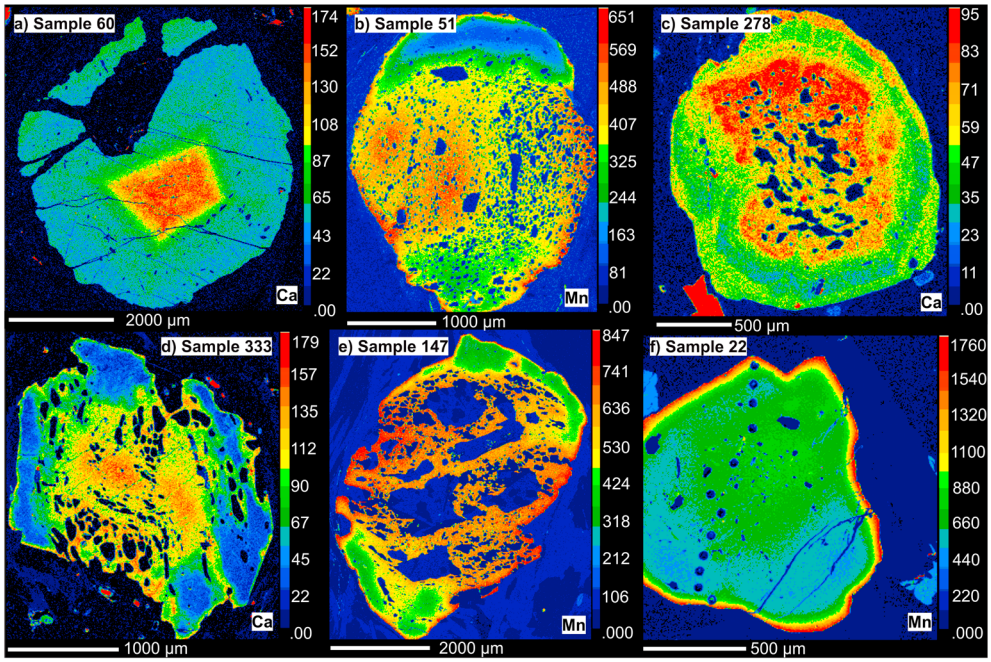

Figure 3. Major element garnet maps: (a) Sample 60, Ca map; (b) sample 51, Mn map; (c) sample 278, Ca map; (d) sample 333, Ca map; (e) sample 147, Mn map; and (f) sample 22, Mn map.

appear to have been partially resorbed, marked by a narrow Mn enrichment zone (Figure 3b). Sample 147 contains large sparse garnet grains in compositional bands. The garnets contain large (~90% total volume), partially resorbed inclusion-filled cores, with an average composition $X_{Ca} = 0.03$, $X_{Mg} = 0.12$, $X_{Fe} = 0.81$, $X_{Mn} = 0.05$, and an asymmetric Mn-poor ($X_{Mn} = 0.02$) overgrowth, probably associated with resorption of the garnet along the foliation surfaces and growth of the asymmetric rim material during pressure shadow development [*Jessup et al.*, 2008] (Figure 3e). Garnets in sample 22 are only weakly zoned in major elements, probably due to their small size (<1 mm), which appears to have allowed partial homogenization of original zoning by diffusion, and have an average composition of $X_{Ca} = 0.05$, $X_{Mg} = 0.15$, $X_{Fe} = 0.73$, and $X_{Mn} = 0.06$. A Mn enrichment is preserved in the outer ~50 µm of the rim, where $X_{Mn} = 0.1$ (Figure 3f).

Garnet grains in samples 60, 278, and 333 preserve distinct major element zoning patterns (Figure 3 and Figures S4–S5 in the supporting information). Garnets in sample 60 preserve partially resorbed cores (Figure 3a), with the composition $X_{Ca} = 0.06$, $X_{Mg} = 0.10$, $X_{Fe} = 0.80$, and $X_{Mn} = 0.04$, overgrown by an inclusion-filled rim of composition $X_{Ca} = 0.02$, $X_{Mg} = 0.15$, $X_{Fe} = 0.82$, and $X_{Mn} = 0.01$. Garnet grains in sample 278 show strong zoning in Ca, with a partially resorbed, synkinematic inclusion-rich core of composition $X_{Ca} = 0.35$, $X_{Mg} = 0.14$, $X_{Fe} = 0.79$, and $X_{Mn} = 0.03$. A chemically distinct rim of composition $X_{Ca} = 0.02$, $X_{Mg} = 0.15$, $X_{Fe} = 0.80$, and $X_{Mn} = 0.03$ overgrew the resorbed core (Figure 3c). Garnets in sample 333 show partially resorbed synkinematic inclusion-filled cores with an average composition of $X_{Ca} = 0.05$, $X_{Mg} = 0.16$, $X_{Fe} = 0.76$, and $X_{Mn} = 0.03$. The rims, with compositions $X_{Ca} = 0.03$, $X_{Mg} = 0.14$, $X_{Fe} = 0.79$, and $X_{Mn} = 0.02$, preserve an ~25–50 µm Mn-enriched ($X_{Mn} = 0.04$) outer layer (Figure 3d).

Matrix biotite has an average composition of $X_{Mg} = 0.44$ in samples 51, 60, and 147; $X_{Mg} = 0.45$ in samples 22 and 147; and $X_{Mg} = 0.47$ in sample 278 (Table S3 in the supporting information).

The samples collected for $^{40}Ar/^{39}Ar$ dating (samples 21, 22, SK-2H, and SK-63) are also kyanite- and sillimanite-bearing metapelites. These micaceous rocks contain one major muscovite population which forms the main penetrative foliation formed during MCT shearing, with average compositions of 6.2–6.42 Si per formula unit (pfu) and 0.08–0.09 Ti pfu for all samples.

4.2. P-T Conditions

P-T conditions along the prograde path were calculated from sample 60, which preserves the strongest garnet prograde zoning patterns. Although samples 278 and 333 also preserve prograde garnet zoning (Figure 3), we

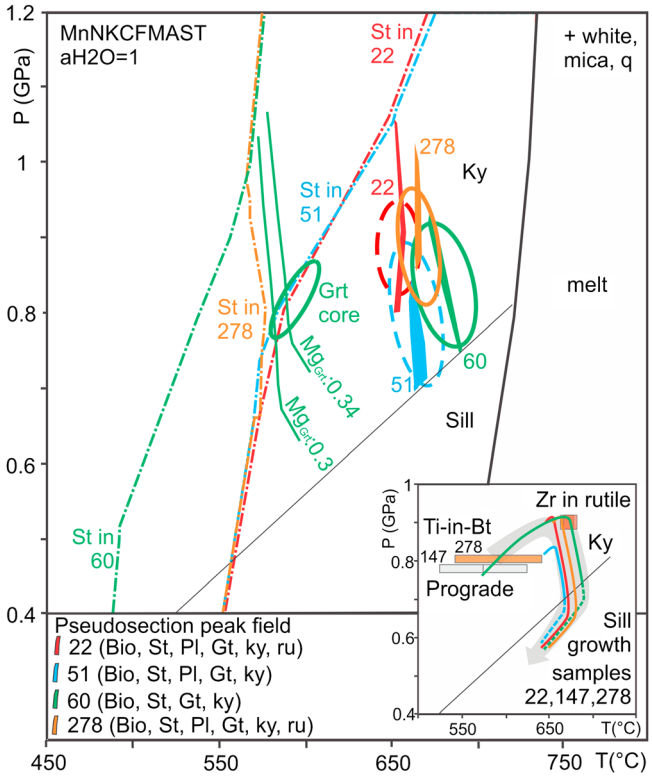

Figure 4. Summary of the P-T history of all samples. Pseudosection peak assemblage fields are shown as colored boxes (samples 60, 51, 278, and 22). The inset shows the Zr-in-rutile [*Tomkins et al.*, 2007] temperatures (calculated at 0.9 GPa pressure) for samples 278, 333, and 22, and Ti-in-biotite [*Henry et al.*, 2005] estimates for samples 147 and 278 (errors = ±50°C). The schematic P-T loop for all samples is shown as a grey arrow. The prograde history is determined from sample 60 (as defined by the garnet core Mg isopleths shown in green). The retrograde path is based on fibrolite present in samples 147 and 22. The staurolite (color-coded by sample), kyanite, and sillimanite-in isograds are shown. The solid line shows the solidus. Bt = biotite, St = staurolite, Pl = plagioclase, Gt = garnet, Ky = kyanite, Ru = rutile, and Sil = sillimanite.

were unsuccessful at modeling a realistic pseudosection for the prograde equilibrium bulk composition for these samples. The successful pseudosection for sample 60, however, shows that garnet cores formed at ~550°C and 0.8 GPa [*Mottram et al.*, 2014b] (Figure 4). There could be potential misrepresentation of the P-T paths of other samples by interpreting the prograde path of all samples based only on this single sample. However, TiB temperature estimates from biotite included in the garnet cores of samples 147 and 278 yield temperatures of 567 ± 50°C and 588 ± 50°C, respectively, within error of this T estimate.

Peak metamorphic conditions of samples 60, 51, 278, and 22 are constrained at ~650–675°C and 0.8–1.0 GPa [*Mottram et al.*, 2014b] (Figures 4 and 5). These pressure estimates are significantly higher than the ~0.4–0.5 GPa calculated for similar grade rocks in the Sikkim Himalaya [*Gaidies et al.*, 2015], indicating a possible overestimation in our calculations. Similar temperatures are however yielded from average P-T estimates (616–680 ± 50°C; Table 1) and Zr-in-rutile thermometry (~675 ± 10°C; Table 1, Figure 4, Figures S6 and S7 in the supporting information).

Constraints on the retrograde path were inferred from sillimanite needles in samples 147 and 22 (Figure 2). Despite the absence of sillimanite and fibrolite in other samples described here, both minerals are observed in rocks immediately adjacent to samples 60, 51, and 278 (samples 57 and 275 from *Mottram et al.* [2014a]). This observation suggests that these rocks passed through the sillimanite field during their exhumation (Figure 4); the growth of sillimanite may have been inhibited in some samples by the nucleation energy required during a period of decreasing temperature on the retrograde path or that sillimanite may have broken down to white mica during retrograde metamorphism.

In summary, these data demonstrate that samples collected from the same structural levels within the thrust zone, but at different locations, experienced peak metamorphic conditions that overlap within ±50°C and ±0.1 GPa.

4.3. U-Th-Pb Geochronology

Monazite dates range between ~21 and 14 Ma in the southern leading edge MCT exposure (samples 333, 147, and 22); between ~21 and 13 Ma, in the central MCT section, 25 km to the north (sample 278); and between ~13 and 12 Ma in the northern rear edge of the MCT (samples 60 and 51; Data Set S1, Figures 6 and 7, Figures S8 and S9, and Tables in the supporting information).

Monazites in sample 60 [*Mottram et al.*, 2014b], which are found in distinctive petrographic locations (Figures 6 and 7a), yielded age populations of 13.2 ± 1.2 Ma (grains included within garnet and staurolite;

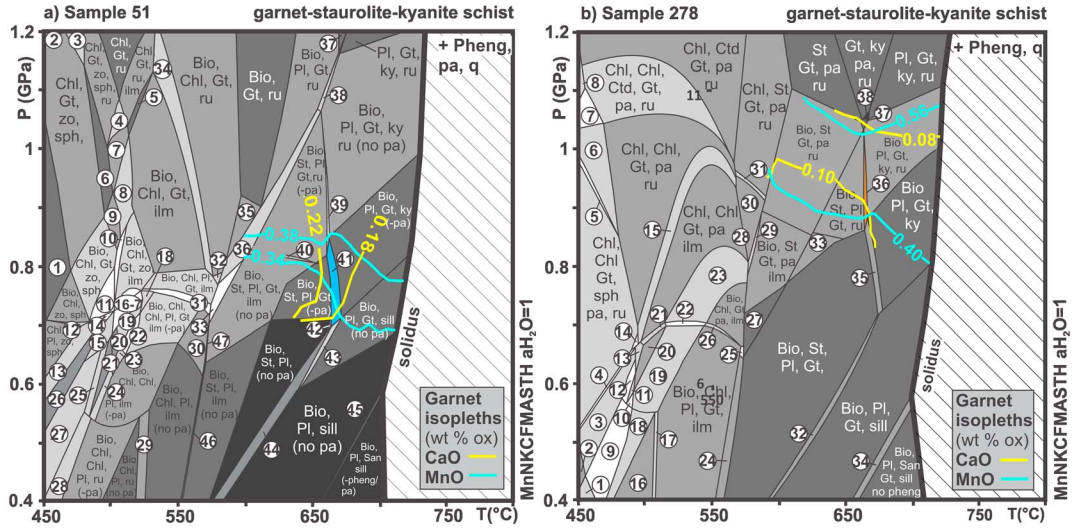

Figure 5. Pseudosections of samples (a) 51 and (b) 278. The peak field is shaded for each pseudosection. Compositional garnet isopleths constrain the peak assemblage (full pseudosections in Table S7 in the supporting information). Samples are modeled in the system MnNKCFMASTH under H_2O-saturated conditions. The area above the solidus for these samples is shown as a hatched area as not modeled. Phases in saturation are shown in the top right of each diagram. (Figure 5a) Pseudosection for sample 51 peak field is shaded in blue (Biotite, Staurolite, Plagioclase, Garnet, and kyanite—field 41). (b) Pseudosection for sample 278 has the peak field shaded in green (Biotite, Staurolite, Plagioclase, Garnet, kyanite, and rutile—field 36).

6 analyses), 13.0 ± 0.5 Ma (grains included within staurolite; 6 analyses), and 12.1 ± 0.7 Ma (matrix grains; 5 analyses [*Mottram et al.*, 2014b]), consistent with their inclusion relationships.

Monazite grains in sample 51 yielded a spread in ages (Figure 6), with populations that may be distinguished by their Y concentrations. The low-Y matrix monazite cores and monazite inclusions within the garnet cores yielded a population age of 13.3 ± 0.1 (14 analyses). High-Y matrix monazite grains yielded an age population of 12.7 ± 0.1 (10 analyses). Two monazite grains included in the garnet rim yielded ages of ~11.5 Ma (Figure 7).

Sample 278 yields several monazite populations that are distinguishable by their inclusion relationships [*Mottram et al.*, 2014b]. Monazites included in the garnet core yielded an age of 20.7 ± 2.2 Ma (4 analyses), inclusions in the mantle yielded an age of 17.9 ± 0.5 Ma (3 analyses), and inclusions in the rim yielded an age of 15.8 ± 1 (4 analyses). Monazite included in kyanite yielded an age of 14.5 ± 0.5 (5 analyses), and those included in staurolite yielded an age of 13.1 ± 0.5 Ma (7 analyses).

Two monazite core analyses in sample 333 yielded a date of ~20 Ma (Figure 7). Further monazite core analyses and monazite grains included in garnet yielded an age of 18.9 ± 1.4 Ma (10 analyses), and a matrix monazite population yielded an age 17.2 ± 0.9 Ma (11 analyses; Figure 6).

Table 1. Summary of Pressure and Temperature Determinations

Sample	Average P-T Temp. (°C)	Average P-T Pressure (GPa)[c]	Zr-in-Rutile (°C)	Pseudosection Peak Field Conditions Temp. (°C)	Pseudosection Peak Field Condition Pressure (GPa)	Pseudosection Prograde History	Ti-in-Biotite (for Prograde History) (°C)[d]
22	642[a]	1.0[a]	675 ± 10	~650	0.8–1.0		
51	616[a]	0.85[a]		~665	0.7–0.9		
60	644[b]	0.9[c]		~675	0.7–0.9	~550°C and ~0.8 GPa	
147	580[a,e]	0.65[a]					567
278	617[a]	0.7[a]	671 ± 14	~670	0.8–1.0		588
333	680[b]	0.8[c]	683 ± 10				

[a]Garnet-biotite-Al_2SiO_5-Plagioclase. [*Holdaway*, 2000] (±50°C/0.12 GPa).
[b]Garnet-biotite thermometer. [*Bhattacharya et al.*, 1992] (±50°C).
[c]Garnet-Al_2SiO_5-Ilmenite.
[d][*Henry et al.*, 2005] (±50°C from biotite grains included within garnet).
[e]The sample is compositionally banded, so it is likely that garnet, biotite, plagioclase, and sillimanite are not in equilibrium. This estimate is therefore taken from a biotite inclusion within garnet to estimate the temperatures of prograde metamorphism.

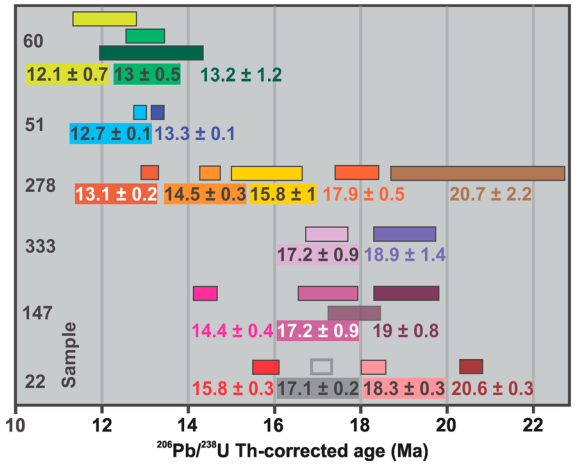

Figure 6. Plot of Th-corrected weighted average $^{206}Pb/^{238}U$ ages for all monazite age populations. All analyses are shown at 2σ error boxes. Monazite dates are corrected for common Pb and Th disequilibrium (details in Text S1.4 in the supporting information; full data shown in Data Set S1 in supporting information).

Sample 147 contains two monazite grains which yielded an age of ~20 Ma (Figure 7). Monazite cores yielded 19 ± 0.8 Ma (8 analyses). A second Th-zoned monazite population included within plagioclase grains yielded an age of 17.2 ± 0.9 Ma (4 analyses), and a high-Y rim population yielded an age 14.4 ± 0.4 Ma (5 analyses; Figure 6).

Sample 22 [*Mottram et al.*, 2014b] yielded a spread in ages between core analyses which yielded a spread of ages between 20.6 ± 0.3 and 18.3 ± 0.3 Ma (25 analyses) and rim analyses which yielded an age of 15.8 ± 0.3 Ma (8 analyses) (Figure 6) [*Mottram et al.*, 2014b].

In summary, while the P-T calculations suggest a similar metamorphic history for all analyzed samples, the timing of metamorphism is strongly related to sampling location, with the youngest ages being obtained from the northern rear edge of the MCT thrust zone, and progressively older ages being derived from localities to the south.

4.4. Trace Element Geochemistry

Monazite and garnet trace element data for samples are presented in Figures 8 and 9 (and Data Set S2 in the supporting information). Monazite grains in all samples record a general trend of heavy rare earth element (HREE)-Y enrichment in the rims relative to the cores. In contrast, garnet cores are relatively enriched in HREE compared to the rims (Figure 8). Garnet grains in samples 60 and 333 are strongly zoned in Y in comparison to other samples (Figure 9). Results for samples 22 and 60 (Figures 8a, 8f, 9a, and 9f) are presented in *Mottram et al.* [2014b].

Monazite rims in sample 51 are enriched in HREE-Y (average $Dy_N/Yb_N = 55$; Y = ~10,000 ppm) in comparison to the cores (average $Dy_N/Yb_N = 140$; Y = ~700 ppm). Garnet grains have flat Y profiles with an average Y content of 400 ppm and a Dy_N/Yb_N ratio of 0.6–1.4 (Figures 8b, 8h, and 9b).

In sample 278, monazite inclusions in kyanite are relatively more enriched in HREE-Y (average $Dy_N/Yb_N = 17$; Y = ~21,000 ppm) than those included within staurolite (average $Dy_N/Yb_N = 69$; Y = ~4500 ppm) and in the matrix (average $Dy_N/Yb_N = 28$; Y = ~12,000 ppm; Figures 8c and 8g). In contrast to the major element zoning patterns, garnet grains contain limited trace element zoning, with an average Y content of 250 ppm and a range in Dy_N/Yb_N from 0.5–3 (Figures 8h and 9c).

To the south, monazite grains in sample 333 show a smaller spread in trace element concentrations, with an average Dy_N/Yb_N of 30–70 (Figures 8d, 8g, and 9d). Garnet grains are strongly zoned in Y (Figure 9d), with rims containing ~50 ppm and the cores ~1500 ppm Y (Figure 8h). Garnet Dy_N/Yb_N ratios range from 0.9 to 4 (Figure 8d).

Sample 147 contains monazite grains that yield a small spread in trace element concentrations with Dy_N/Yb_N ranging from 13 to 27 from rim to core. Garnet cores have a fairly flat Y profile with an average composition of 300 ppm Y (Figure 8h). Garnet rims are relatively more depleted in HREE in comparison to the cores, with average Dy_N/Yb_N ratios of 4.2 and 0.4, respectively (Figures 8e, 8g, and 9e).

4.5. Petrochronology

Petrochronology provides a means to link accessory mineral age to the metamorphic stage in which it grew [e.g., *Kohn et al.*, 2004; *Kylander-Clark et al.*, 2013; *Mottram et al.*, 2014b, and references therein]. The REE-Y budget of a rock is strongly controlled by the differential growth and dissolution of accessory phases such as monazite, allanite, xenotime, and apatite and major phases such as garnet. The age to stage linkage can therefore be formed through investigating the textural (inclusion) relationships [e.g., *Janots et al.*, 2009, and references therein] and/or by using trace element fingerprints in monazite and other major phases

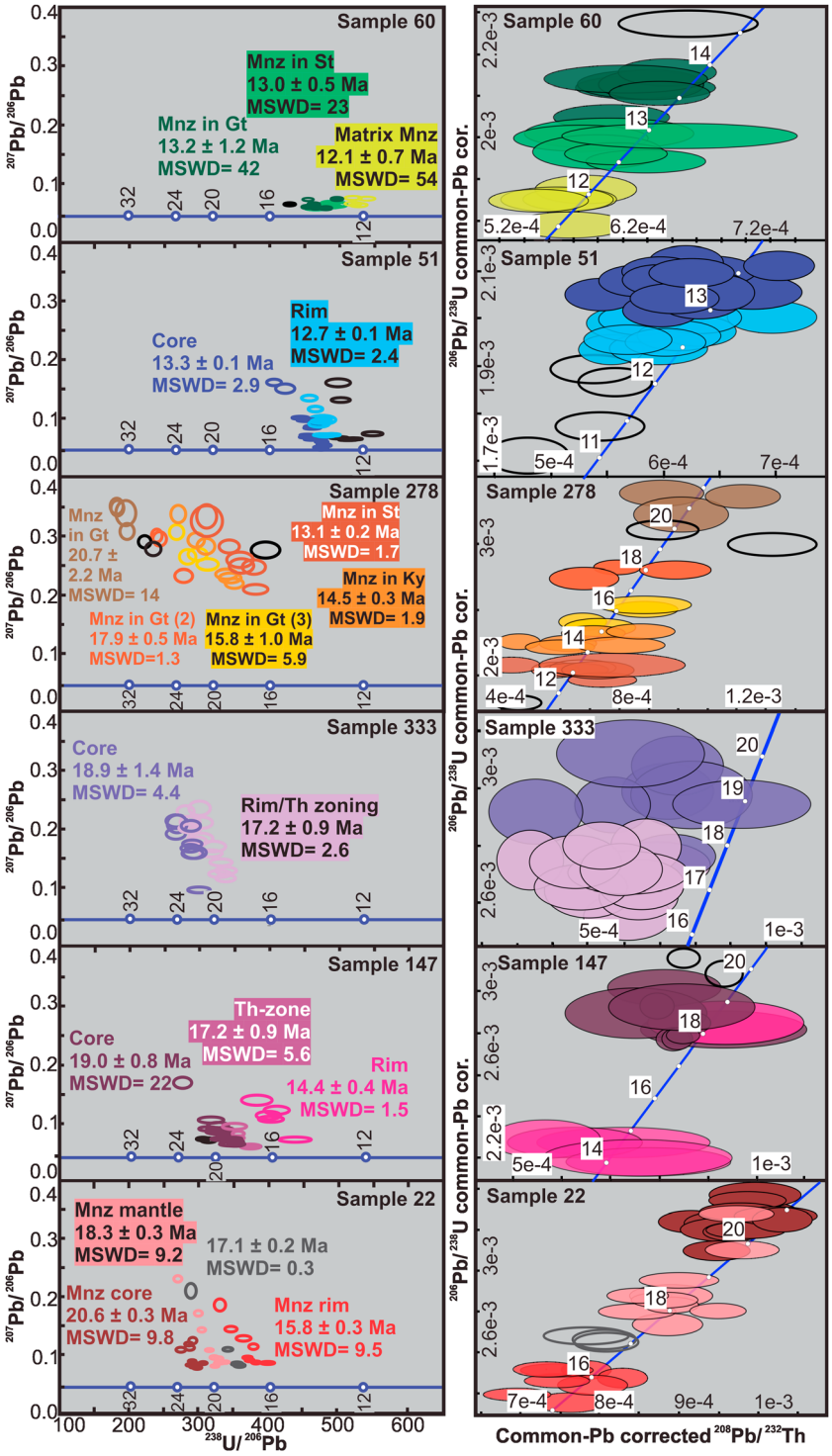

Figure 7. Tera-Wasserburg and Th-Pb plots of monazite data (samples 60, 51, 278, 333, 147, and 22). All analyses shown at 2σ error ellipses. All data shown on the Tera-Wasserburg plots are uncorrected for common Pb; quoted ages are average common Pb- and Th-corrected $^{238}U/^{206}Pb$ ages (intercept ages are shown in Figure S9.1 in the supporting information). Monazite populations (shown in different colors) based on either petrological or chemical zoning controls. Data plotted on Th-Pb plots are corrected for both common Pb ($^{208}Pb/^{232}Th$) and common Pb and Th disequilibrium ($^{206}Pb/^{238}U$, details in Text S1.4 in the supporting information; full data in Data Set S1 in supporting information; uncorrected Th-Pb plots are shown in Figure S9 in the supporting information.

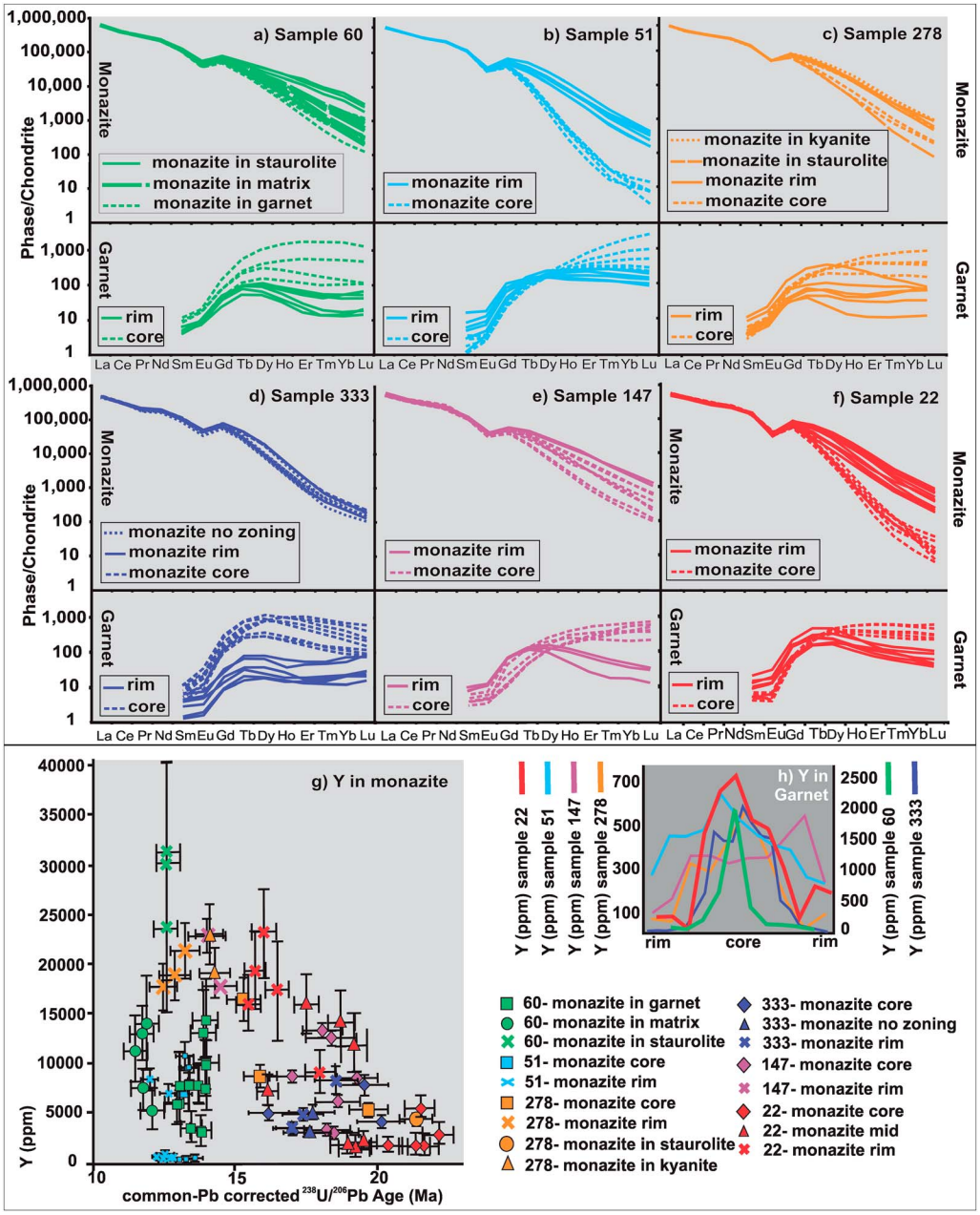

Figure 8. Monazite and garnet REE geochemistry for all samples normalized to Chondritic values of *McDonough and Sun* [1995]. (a) Sample 60; (b) sample 51; (c) sample 278; (d) sample 333; (e) sample 147; (f) sample 22; (g) Y content of monazites for all samples (legend to right); and (h) Y in garnet transects for all samples, Y content for samples 51, 278, 147, and 22 on the left axis, and samples 60 and 333 on the right axis. Full trace element data set can be found in the supporting Data Set S2.

such as garnet to track the minerals' reaction history [e.g., *Hermann and Rubatto*, 2003; *Rubatto et al.*, 2006] (Figures 8–10).

In sample 51 (Figure 10a), the timing of prograde metamorphism is constrained by the growth of HREE-Y-depleted monazite cores at 13.3 ± 0.1 Ma. Allanite, commonly destabilized during garnet growth [*Janots et al.*, 2008], provides a likely light rare earth (LREE) element source for the HREE-Y-depleted monazite cores and further grains included within the prograde, synkinematic, garnet inclusion trails. The timing of peak metamorphic conditions is constrained by the growth of HREE-Y-enriched monazite rims at 12.7 ± 0.1 Ma. On the prograde path, near-peak conditions, garnet isomodes (Figure S7.3.2.4 in the supporting information) are parallel to the P-T path, meaning that garnet experienced a hiatus in growth, or was breaking down at

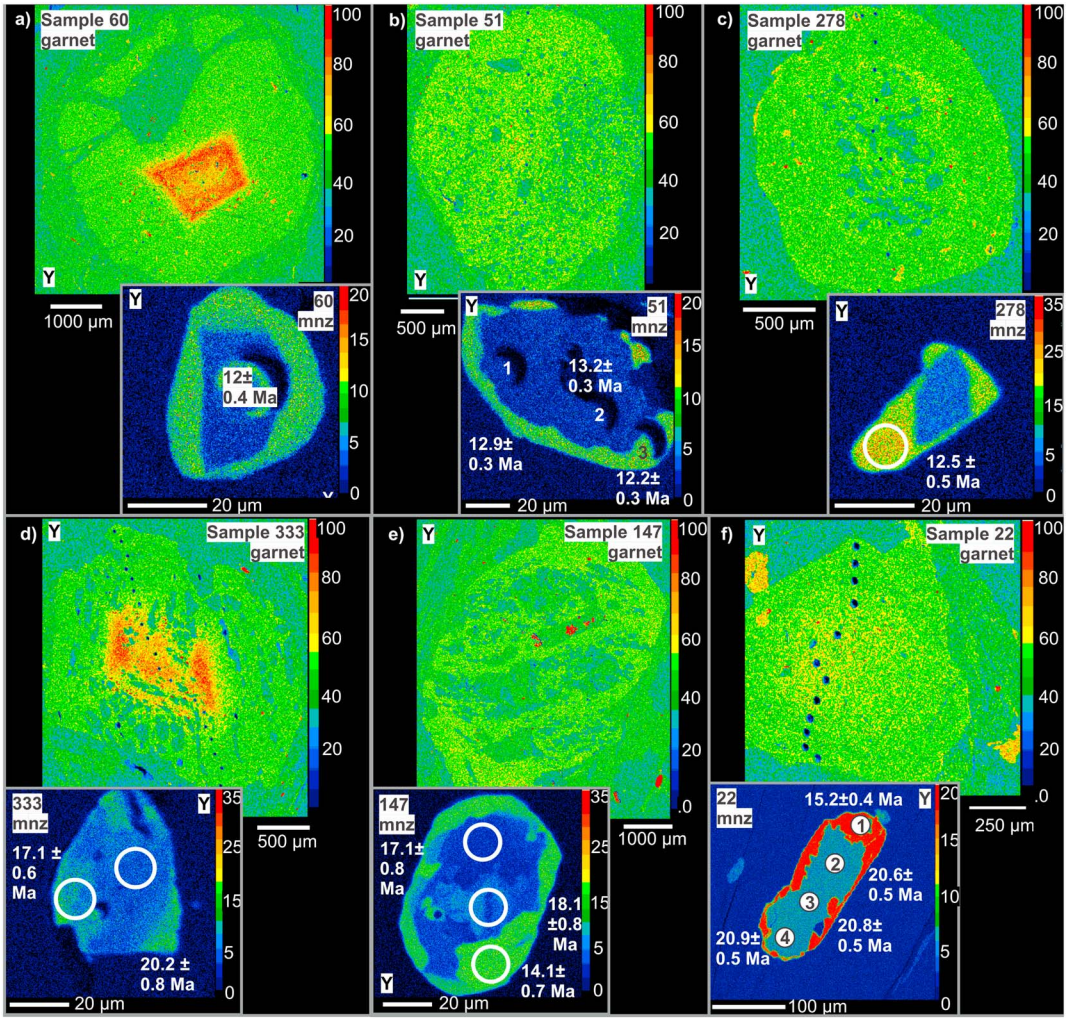

Figure 9. Y maps for garnet and monazite. (a) Sample 60, (b) sample 51, (c) sample 278, (d) sample 333, (e) sample 147, and (f) sample 22. Ages are Th-corrected $^{238}U/^{206}Pb$ ages.

this point. The HREE-Y-enriched monazite rim was therefore likely to have formed during this time of low competition for REE. Monazite included in Mn-poor asymmetric garnet rims yield an age ~11 Ma, suggesting continued metamorphism and postpeak garnet growth until after this time. Similar HREE-Y core rim garnet and monazite links in sample 22 were described by *Mottram et al.* [2014b].

The multiple monazite populations in sample 278 (Figures 6 and 10b) can be linked directly to the textural context in which each grain is found: populations of different age are located in garnet, kyanite and staurolite, and in the matrix. Monazite included in garnet yields ages from 20.7 ± 2.2 in the core to 17.9 ± 0.5 Ma in the mantle and 15.8 ± 1 Ma in the rim, thus constraining the timing of garnet growth to between <21 Ma and >16 Ma. The timing of prograde metamorphism is constrained between 17.9 ± 0.5 Ma and 15.8 ± 1 Ma, when the garnet core and mantle were forming, enveloping earlier-formed monazite grains. The HREE-Y-depleted matrix monazite cores crystallized in the presence of garnet at this time.

Peak metamorphism occurred at conditions of 670°C and 0.8–1.0 GPa (Figure 5), an estimate supported by Zr-in-rutile temperatures of 671 ± 14°C (Table 1) from rutile grains included within the garnet rim (suggesting that peak temperatures were reached prior to outer garnet rim growth). The sample experienced peak conditions between 14.5 ± 0.5 Ma and 13.1 ± 0.5 Ma, as documented by the age of monazite inclusions in kyanite and staurolite. Monazite growth at 14.5 ± 0.5 Ma may represent a break in garnet growth, evidenced by the preferential incorporation of HREE and Y into the monazite generation now preserved in kyanite and the outer garnet rim. This occurred during the hiatus in garnet growth on the

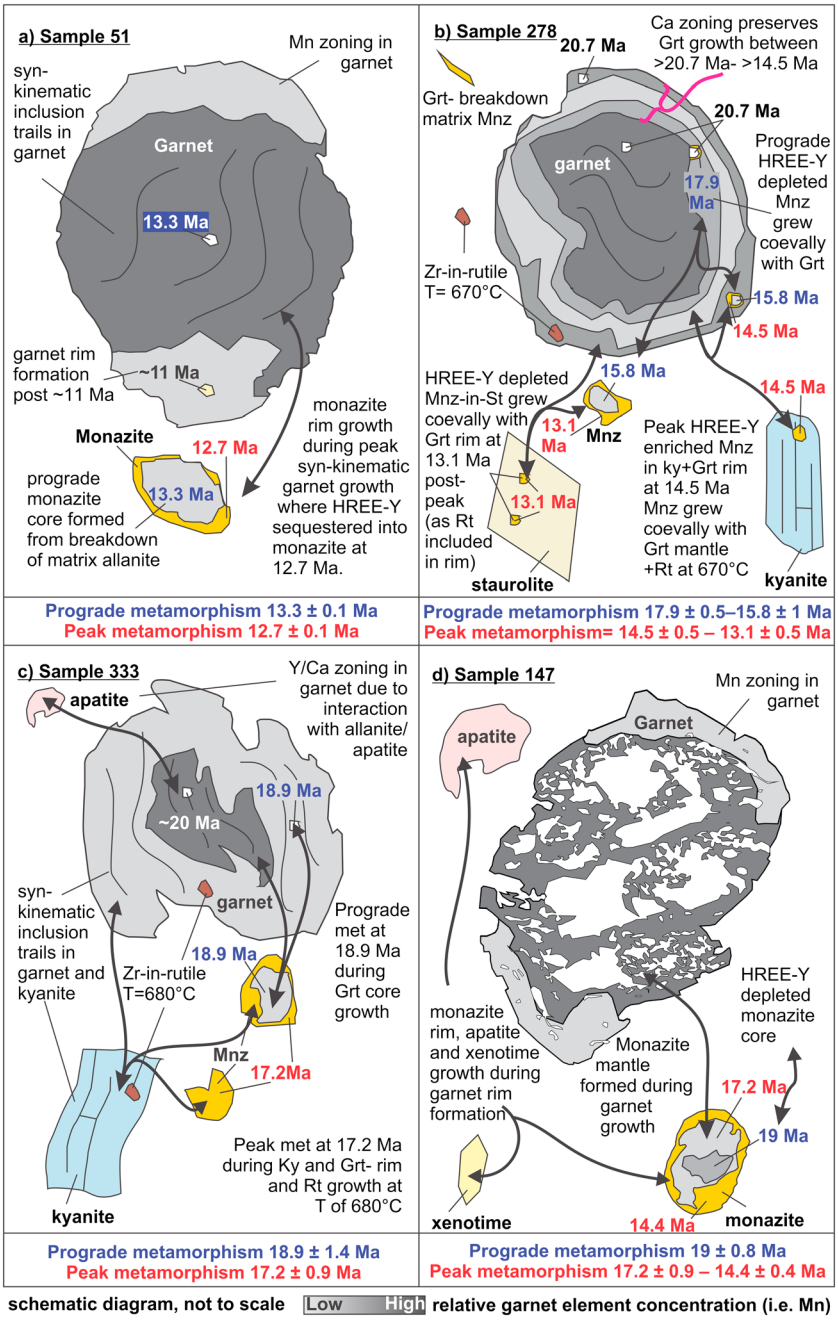

Figure 10. Petrochronological interpretation of sample age to stage linkages. Schematic cartoons illustrating the major reactions which have occurred in the rocks (not to scale). (a) Sample 51, (b) sample 278, (c) sample 333, and (d) sample 147. Relative element zoning is shown in grey (light = low concentrations; dark = high concentrations). HREE-Y zoning in monazite is shown with yellow = high HREE-Y and grey = low HREE-Y.

prograde path, near-peak conditions, evidenced by P-T path-parallel garnet isomodes (Figure S7.3.4.4 in the supporting information). The 13.1 ± 0.5 Ma population represents the subsequent initiation of growth of the outer garnet rim, evidenced by the P-T path passing through the steeply inclined isomodes, indicating garnet growth. At this time, the HREE and Y were preferentially sequestered into garnet, forming the relatively depleted HREE-Y monazite population now preserved in staurolite. The breakdown of another accessory phase such as apatite could have caused the middle rare earth element (MREE)-enrichment in the garnet rim and provided the phosphorous to form monazite (Figure 10b). These inclusion-relationship observations are similar to those for sample 60, documented by *Mottram et al.* [2014b].

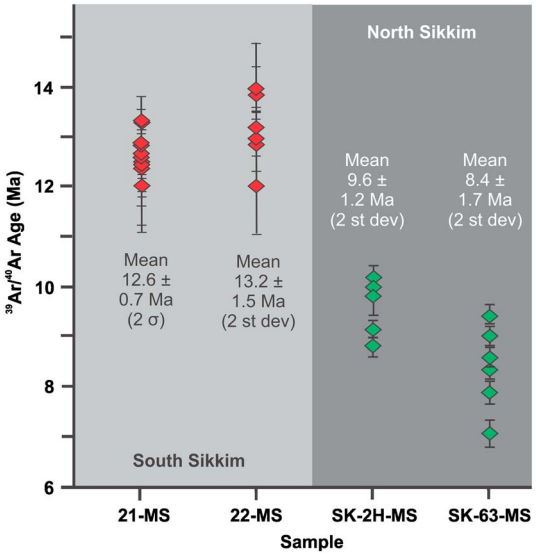

Figure 11. The ^{40}Ar/^{39}Ar single grain fusion plots for samples 21 and 22 (south) and samples SK-2H and SK-63 (north). Errors are 2 standard deviation.

Monazite in sample 333 (Figure 10c) yielded a more limited spread in REE and Y concentrations than the other samples (Figure 8d). Similar to sample 60 [*Mottram et al.*, 2014b], garnet displays strong Ca-Y zoning, possibly due to elemental competition with allanite or apatite during growth along the prograde path. The breakdown of these minerals (now no longer present in the matrix) may have caused the MREE enrichment in garnet rim. The timing of prograde metamorphism is constrained by 18.9 ± 1.4 Ma monazite grains included in the synkinematic garnet inclusion trails. The timing of peak metamorphism is recorded by the 17.2 ± 0.9 Ma matrix monazite grains which probably grew during kyanite and garnet rim crystallization at peak conditions of 683 ± 10°C (Zr-in-rutile concentrations from rutile both included in the garnet rim and within the matrix; Table 1 and Figure 4).

Sample 147 contains large, but sparsely distributed, inclusion-rich and Mn-zoned garnet grains (Figures 3e and 9e), which are separated from the plagioclase crystals, located in chemically distinct bands. The timing of prograde metamorphism is obtained from the 19 ± 0.8 Ma HREE-Y-poor monazite core population. The timing of peak metamorphism is more difficult to constrain due to the chemical banding of the sample and could be represented by either the 17.2 ± 0.9 Ma monazites located within plagioclase grains or the 14.4 ± 0.4 Ma monazite rims. The presence of large xenotime grains in the matrix provides evidence for Y release during garnet breakdown, which may also have facilitated growth of the youngest monazite population during this time (Figure 10d). Ti-in-biotite temperatures of 567 ± 50°C yielded from grains included within garnet (Table 1) suggests that this sample may have spent more time at lower grade conditions than others in this study.

4.6. ^{40}Ar/^{39}Ar Geochronology

The four samples selected for ^{40}Ar/^{39}Ar dating yielded muscovite single-grain fusion ages which span ~2–3 Ma for each sample (Figure 11; full data set is presented in supporting Data Set S3). Samples SK-2H and SK-63 from northern Sikkim yielded mean ages of 9.6 ± 1.2 Ma (2σ) and 8.4 ± 1.7 Ma (2σ). In contrast, the samples from the south of the Sikkim Himalaya (samples 21 and 22) yielded mean ages of 12.6 ± 0.7 Ma (2σ) and 13.2 ± 1.5 Ma (2σ; Figure 11). Hence, there is a distinct trend from significantly younger ages in the northern rear edge of the MCT zone toward older ages at the southern leading edge. This spatial trend mimics that observed from monazite ages (Figure 6).

5. Discussion

5.1. Time Windows Into Ductile Thrusting History

In summary, the ages of monazite growth during analogous P-T path conditions from multiple similar grade metamorphic samples separated by >50 km along the transport direction of the MCT vary by ≥8 Ma, with youngest ages to the north. Burial, metamorphism, and deformation therefore occurred earlier in samples from the southern, leading edge of the thrust sheet than samples from farther north. The southern samples (333, 147, and 22) were buried, accreted to the hanging wall between ~21 and 14 Ma, and continued to deform during exhumation, recorded by the ^{40}Ar/^{39}Ar muscovite cooling ages of ~13 Ma (Figure 12a). The midwesterly sample 278 was accreted to the hanging wall after burial to the same ductile conditions between ~21 and 13 Ma, and northeasterly rear-edge samples 60 and 51 were buried and accreted over a shorter time period, between ~13 and 12 Ma (Figure 12b) and began to cool during exhumation by ~9 Ma. These data demonstrate a progressive evolution of thrust-related metamorphism from south to north within the ductile thrust zone of the MCT.

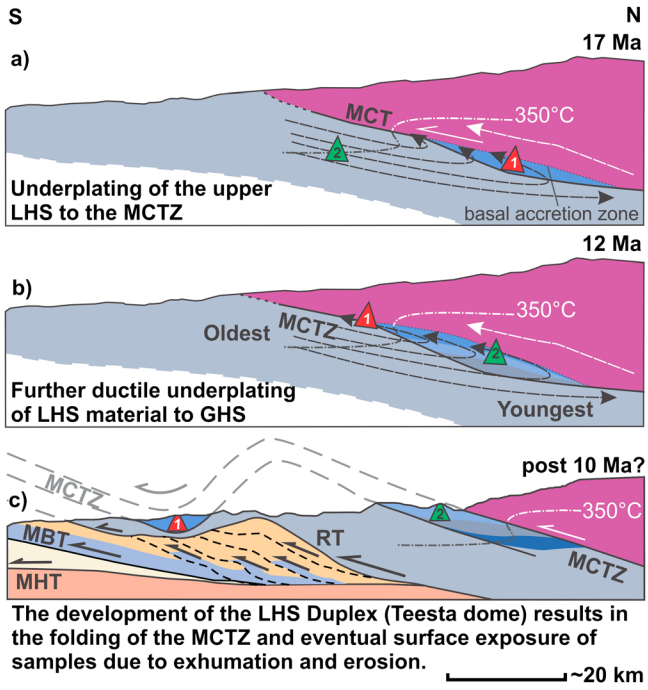

Figure 12. Schematic cross sections showing the evolution of the MCT through time (legend same as Figure 1): (a) Underplating of the upper LHS from the footwall to the hanging wall of the MCT in a zone of accretion associated with a ramp on the paleo-MCT. The triangle 1 represents location of samples 333, 147, and 22 from the south of Sikkim. (b) As the MCT evolved, there was continued underplating of upper LHS material into the hanging wall of the structure, forming the MCT zone (MCTZ). Triangle 2 represents this later accretion of samples from the north of Sikkim (samples 60 and 51). (c) The development of the Teesta dome due to later brittle duplexing in the LHS material below the Ramgarh Thrust (RT) folded the resulting in the exposure at the surface of both triangles 1 and 2, which originally represent different time slices of the MCT evolution.

This process occurred during a scenario where the Lesser Himalayan Indian plate material, buried in the footwall of the MCT, was subsequently underplated to the MCT hanging wall in a basal accretion zone associated with a ramp on the MCT [e.g., *Catlos et al.*, 2001; *Harrison et al.*, 1997, 1998; *Kohn et al.*, 2001; *Larson et al.*, 2013; *Mottram et al.*, 2014b]. Peak metamorphism in the MCT zone developed from heat advected downward from the overriding GHS material. The thrusting of hotter over colder material led to the perturbation of isotherms along the thrust zone [*e.g., Bollinger et al.*, 2004; *Henry et al.*, 1997; *Huerta et al.*, 1998, 1999] and the development of an inverted metamorphic sequence when slivers of (footwall) LHS material were progressively and continuously accreted into the MCT hanging wall of the thrust zone [*Bollinger et al.*, 2006; *Herman et al.*, 2010, Figures 12a–12b].

Subsequent, late-stage exhumation was caused by the formation of the Lesser Himalayan Duplex (LHD) beneath the MCT zone, dated at $<$10 Ma in neighboring Bhutan [*McQuarrie et al.*, 2014]. This process is associated with the foreland migration of fault structures and caused the southerly exposed Sikkim Himalaya rocks to be exhumed to shallower levels by ~13 Ma and the more northerly exposed rocks to be exhumed by ~9.5–8.5 Ma, as documented by the muscovite $^{40}Ar/^{39}Ar$ ages. Once these rocks had been exhumed, erosion by the Teesta River exposed the different time windows into the MCT evolution at the surface (Figure 12c).

The data reveal that at various stages throughout the thrusting and the exhumation history, samples from the leading and rear edge of the thrust zone were separated by a $>$5 Ma time interval. This in turn suggests that thrusting and exhumation along the MCT was a broadly continuous process, at least between ~22 Ma and ~9 Ma. A steady state configuration of thermal, metamorphic, and deformation conditions, with respect to the surface and frontal portion of the thrust, could have existed, as implied in numerical models [e.g., *Bollinger et al.*, 2004; *Henry et al.*, 1997], and this scenario appears consistent with our data.

This study demonstrates that doming of major ductile shear zones such as the MCT can be exploited to reveal the duration during which these zones were active. Differences in U-Th-Pb monazite and muscovite $^{40}Ar/^{39}Ar$ ages from foreland- and hinterland-located GHS rocks in the Everest region [*Cottle et al.*, 2009] and the LHS rocks in the Garwhal Himalaya [*Celerier et al.*, 2009], respectively, demonstrate that differing erosion horizons are probably ubiquitous along orogenic strike. Furthermore, our findings suggest that the range of monazite age data from different locations along strike of the MCT [~21–8 Ma; *Catlos et al.*, 2001, 2002; *Daniel et al.*, 2003; *Harrison et al.*, 1997; *Kohn et al.*, 2001; *Tobgay et al.*, 2010] are likely to be partly due to the exposure of different down-dip sections of a long-lived shear zone rather than exclusively recording variations in the timing of its activity along strike.

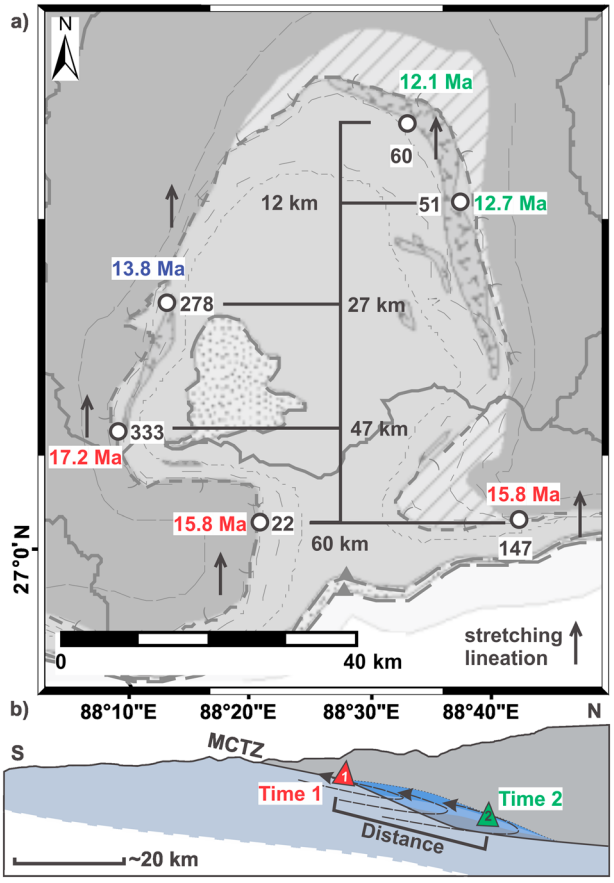

Figure 13. Rates calculation: (a) Map (see Figure 1 for legend) showing the distance measured parallel to the N-S stretching lineation between samples and interpreted peak metamorphic ages—quoted average common Pb and Th-corrected $^{238}U/^{206}Pb$ ages, where ages for samples 147 and 278 are averages of multiple populations (Table S10 in the supporting information). (b) Schematic cross section showing the assumed geometry of the thrust prior to doming. The rate of movement can be calculated by dividing the age difference between samples (T1 and T2) by the distance separating the samples.

5.2. Calculating Rates of Ductile Thrusting

The steady state, continuous thrusting model provides a basis for estimating the rate at which material from the deeper hinterland progressively moved through the thrust zone in the direction of the foreland along similar P-T paths (Figure 13). By assuming a quasi-steady state existed between thermal, metamorphic, and deformational processes relative to both the surface above samples and the frontal part of the Himalaya, a rate of transport relative to steady state isotherms can be calculated. By taking the >5 Ma difference in age of attainment of similar metamorphic conditions, overall between ~21 and 12 Ma, and the transport direction-parallel distance between the samples, a minimum thrusting rate can be calculated (Figure 13). The distance is measured parallel to the N-S stretching lineation and is then multiplied by a factor that takes into account the curvature of the Teesta Dome, by using average foliation dips.

We have regressed the sample age relative to the age of sample 60 (the most rearward sample in terms of direction of thrusting) versus distance between samples, also relative to the position of sample 60 and measured parallel to the N-S stretching lineation, to represent a schematic of the surface of the MCT detachment prior to folding by the underlying LHD (Figure 14 and Table S10 in the supporting information). The regression suggests an average minimum thrusting rate of 10 ± 3 mm yr^{-1} (2σ). The uncertainties are based on the analytical and systematic uncertainties on the age data and maximum and minimum distance estimates (Table S10 in the supporting information).

Our calculated average rate depends on two major assumptions. First, the present-day exposure distance between samples provides only a minimum estimate of their original distance at the time of metamorphism, since the relative displacements within the distributed ductile shear zone associated with the MCT, (Figure 12) [*Mottram et al.*, 2014a, 2014b], or due to ramps on the paleostructure akin to those present on the present-day MHT [e.g., *Coutand et al.*, 2014], may mean that the original distance separating samples was larger. Hence, any thrusting rate calculated from this distance is a minimum estimate.

Second, the assumption of thermal equilibrium between 21 and 12 Ma implies that the isotherms effectively remained stationary with respect to the evolving and eroding mountain front. The virtually identical P-T evolution recorded by the samples at different times suggests that dynamic thermal equilibrium is a reasonable assumption; further support is provided by thermal models that suggest the relative stability of isotherms with distance from the topographic front through time [*Bollinger et al.*, 2004, 2006; *Coutand et al.*, 2014; *Henry et al.*, 1997; *Herman et al.*, 2010; *Whipp et al.*, 2007].

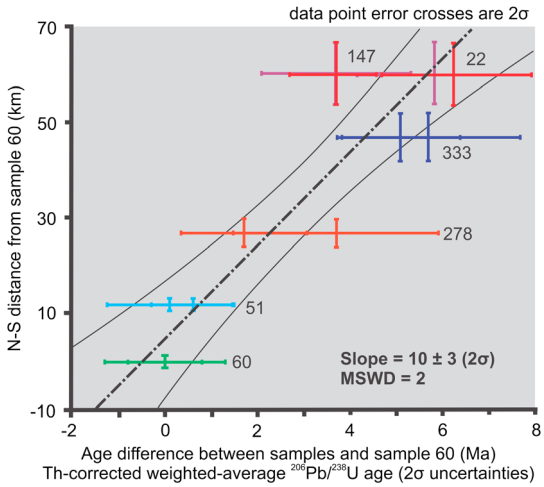

Figure 14. Error-weighted regression plot where prograde and peak monazite ages are plotted on the *x* axis relative to the age of northernmost sample 60. Distances are plotted on the *y* axis, measured parallel to the N-S stretching lineation from the northernmost sample 60, and are increased to accommodate the doming of the MCT. Errors are plotted as 2σ and an uncertainty envelope is included around the regression line (model 2 regression in Isoplot [*Ludwig*, 2003]. The slope of the line is equivalent to the rate of thrusting of 10 ± 3 mm yr^{-1}.

Our data also indicate that the duration of metamorphism is shorter in the younger, northernmost samples, suggesting either (1) a shift in the thermal regime, (2) differences in the accretion mechanism governing the shear zone through time, or (3) LHD initiation caused a shorter period of prograde and peak metamorphism in the rocks at depth within the MCT zone at ~13 Ma (as recorded in the muscovite ^{40}Ar/^{39}Ar ages in the southern MCT exposures). A lack of temporal constraints of uplift of the LHD in the Sikkim Himalaya preclude distinguishing clearly between these scenarios.

Results from thermomechanical modeling, thermochronological data, and studies of foreland basin migration suggest that modern convergence of India and Asia accommodated in the Himalaya is partitioned into two mechanisms: overthrusting of the hanging wall block as material is thrust along fault surfaces at ~5 mm yr^{-1} and underthrusting as material is buried in the footwall of the fault at ~15 mm yr^{-1} [*Avouac*, 2003; *Bollinger et al.*, 2004, 2006; *Coutand et al.*, 2014; *Herman et al.*, 2010]. The partitioning between these two mechanisms may, however, have changed through time. As ductile accretion [e.g., *Bollinger et al.*, 2006] occurs mainly during the overthrusting mechanism, our ~10 ± 3 mm yr^{-1} rate provides some constraints on the importance of this component in influencing the thermal history of these rocks during the Miocene. Underthrusting processes, recorded today in the foreland basins, e.g., *Avouac* [2003], *Burgess et al.* [2012], and *Hirschmiller et al.* [2014] could also have been acting at the time and could be recorded in the prograde history of the Sikkim Himalayan samples.

Our calculated minimum average rate is broadly comparable with estimated rates of 4–11 mm yr^{-1} and 9–19 mm yr^{-1} for the Annapurna MCT section [*Corrie and Kohn*, 2011], 22 mm yr^{-1} for the Langtang section [*Kohn et al.*, 2004], and 36–58 mm yr^{-1} for the western Bhutan section [*McQuarrie et al.*, 2014; *Tobgay et al.*, 2012]. The variation in estimated rates implies either spatial/temporal variations along strike [*Bettinelli et al.*, 2006] or reflects the different methodologies applied. The Annapurna and Langtang estimates [*Corrie and Kohn*, 2011; *Kohn et al.*, 2004] were generated using petrologic and thermal models to provide an estimate of the lateral displacement between faults, with the high rate variation depending on whether the distance calculation was based on the thermal model of *Herman et al.* [2010] or *Bollinger et al.* [2006] and the time period in question. The Bhutan estimates [*McQuarrie et al.*, 2014; *Tobgay et al.*, 2012] were generated by combining distance shortening estimates from balanced cross sections with monazite geochronology. This method relies on several significant assumptions about the geometry of the structures on which the distances are based and about the interpretation of the monazite ages and takes little account of ductile deformation. As such, there are significant uncertainties to this method.

The distance term input into the rate calculation in all methods, including ours, is clearly difficult to constrain accurately. Our approach however provides an estimate of a minimum distance, and the combination of U-Pb and muscovite ^{40}Ar/^{39}Ar data demonstrates that samples >50 km apart experienced similar burial and cooling histories at different times. The exploitation of petrochronological methods on samples exposed across a wide part of the orogen at the same structural level within a ductile fault zone thus provides a new, robust method for estimating minimum average rates of ductile thrusting at midcrustal depths that is independent of stratigraphic uncertainties and the inevitable errors involved in producing restored cross sections.

6. Conclusions

We have exploited a folded ductile thrust zone in the Sikkim Himalaya to provide insight into >10 Ma of the ductile thrusting history of the MCT, one of the key Himalayan structures that accommodated India-Asia convergence during the Miocene. Advances in petrochronological techniques have revealed significant temporal variation within the thrust zone where ductile deformation took place between ~21 and 14 Ma in the southern, leading edge, between ~21 and 13 Ma, in the midsection, and over a shorter time period between ~13 and 12 Ma in the rear edge of the thrust zone, as revealed by U-Th-Pb monazite ages. This >5 Ma spread is also found in the exhumation and cooling history that occurred at ~13 Ma and 8–9 Ma in the disparate parts of the thrust zone, as shown by muscovite $^{40}Ar/^{39}Ar$ data.

These data are used to calculate rates of movement for part of the MCT thrust system, demonstrating that movement occurred at a minimum average rate of $\sim 10 \pm 3\ mm\ yr^{-1}$ during the Miocene. The methodology used could be applied to other areas, both in the Himalaya and in other orogens, to determine the rates of movement of any major thrust or extensional fault exposed over large areas across strike by folding, provided that the uncertainties on age determinations are modest in relation to the age of the deformation. As such, Cenozoic and Mesozoic orogens may be tractable targets of this approach. The determination of rates of ductile shear has major global significance for understanding the mechanism by which ductile movement in the midcrust occurs during continental collision.

Acknowledgments

Supplementary data can be found as a supporting data files. This study was funded by a NERC PhD studentship awarded to C.Mottram (NE/1528018/1), a NERC Advanced Fellowship awarded to C.Warren (NE/HO16279/1) and a Royal Society International Joint Project grant (IJP 2008/R3) awarded to N.Harris, S.Gupta, and T.Argles. Analytical work was funded by a NERC facility grant awarded to N.H and C.M (IP-1129-0511). M.Caddick is thanked for discussion of pseudosections. M.Horstwood, J.Cottle, and C.Spencer are thanked for discussion of geochronological data. Aditi Das is thanked for collecting Ar-Ar data. We thank S. Hammond, A.Tindle, A. Halton, M. Higgins, K. Green, J. Watson, S. Gupta, S. Mitra, L. Greenwood, T. Chopdel, and K. Norgay Sherpa for technical support and help in the field. R.Thigpen and A. Webb are thanked for constructive and helpful reviews of an earlier version of the manuscript. Comments from K. Larson, an anonymous reviewer, and Associate Editor D. Gruijic significantly improved this manuscript.

References

Anczkiewicz, R., S. Chakraborty, S. Dasgupta, D. Mukhopadhyay, and K. Kołtonik (2014), Timing, duration and inversion of prograde Barrovian metamorphism constrained by high resolution Lu–Hf garnet dating: A case study from the Sikkim Himalaya, NE India, *Earth Planet. Sci. Lett.*, *407*, 70–81, doi:10.1016/j.epsl.2014.09.035.

Avouac, J. P. (2003), Mountain building, erosion, and the seismic cycle in the Nepal Himalaya, *Adv. Geophys.*, *46*, 1–80.

Banerjee, P., and R. Bürgmann (2002), Convergence across the northwest Himalaya from GPS measurements, *Geophys. Res. Lett.*, *29*(13), 1652, doi:10.1029/2002GL015184.

Bettinelli, P., J.-P. Avouac, M. Flouzat, F. Jouanne, L. Bollinger, P. Willis, and G. R. Chitrakar (2006), Plate motion of India and interseismic strain in the Nepal Himalaya from GPS and DORIS measurements, *J. Geod.*, *80*(8–11), 567–589.

Bhattacharya, A., L. Mohanty, A. Maji, S. Sen, and M. Raith (1992), Non-ideal mixing in the phlogopite-annite binary: Constraints from experimental data on Mg−Fe partitioning and a reformulation of the biotite-garnet geothermometer, *Contrib. Mineral. Petrol.*, *111*(1), 87–93.

Bhattacharyya, K., and G. Mitra (2009), A new kinematic evolutionary model for the growth of a duplex - an example from the Rangit duplex, Sikkim Himalaya, India, *Gondwana Res.*, *16*(3–4), 697–715.

Bilham, R., K. Larson, J. Freymueller, F. Jouanne, P. Le Fort, P. Leturmy, J. Mugnier, J. Gamond, J. Glot, and J. Martinod (1997), GPS measurements of present-day convergence across the Nepal Himalaya, *Nature*, *386*(6620), 61–64.

Bollinger, L., J. Avouac, O. Beyssac, E. Catlos, T. Harrison, M. Grove, B. Goffé, and S. Sapkota (2004), Thermal structure and exhumation history of the Lesser Himalaya in central Nepal, *Tectonics*, *23*, TC5015, doi:10.1029/2003TC001564.

Bollinger, L., P. Henry, and J. Avouac (2006), Mountain building in the Nepal Himalaya: Thermal and kinematic model, *Earth Planet. Sci. Lett.*, *244*(1), 58–71.

Burgess, P., A. Yin, C. S. Dubey, Z.-K. Shen, and T. K. Kelty (2012), Holocene shortening across the Main Frontal Thrust zone in the eastern Himalaya, *Earth Planet. Sci. Lett.*, *357–358*, 152–167, doi:10.1016/j.epsl.2012.09.040.

Catlos, E. J., T. M. Harrison, M. J. Kohn, M. Grove, F. J. Ryerson, C. E. Manning, and B. N. Upreti (2001), Geochronologic and thermobarometric constraints on the evolution of the Main Central Thrust, central Nepal Himalaya, *J. Geophys. Res.*, *106*(B8), 16,177–16,204, doi:10.1029/2000JB900375.

Catlos, E. J., T. M. Harrison, C. E. Manning, M. Grove, S. M. Rai, M. S. Hubbard, and B. N. Upreti (2002), Records of the evolution of the Himalayan orogen from in situ Th-Pb ion microprobe dating of monazite: Eastern Nepal and western Garhwal, *J. Asian Earth Sci.*, *20*(5), 459–479.

Catlos, E. J., C. S. Dubey, T. M. Harrison, and M. A. Edwards (2004), Late Miocene movement within the Himalayan Main Central Thrust shear zone, Sikkim, north-east India, *J. Metamorph. Geol.*, *22*(3), 207–226, doi:10.1111/j.1525-1314.2004.00509.x.

Celerier, J., T. M. Harrison, O. Beyssac, F. Herman, W. J. Dunlap, and A. A. G. Webb (2009), The Kumaun and Garwhal Lesser Himalaya, India: Part 2. Thermal and deformation histories, *Geol. Soc. Am. Bull.*, *121*(9–10), 1281–1297, doi:10.1130/B26343.1.

Clark, M. K., and R. Bilham (2008), Miocene rise of the Shillong Plateau and the beginning of the end for the Eastern Himalaya, *Earth Planet. Sci. Lett.*, *269*(3), 337–351.

Connolly, J. (1990), Multivariable phase diagrams; an algorithm based on generalized thermodynamics, *Am. J. Sci.*, *290*(6), 666–718.

Connolly, J. (2009), The geodynamic equation of state: What and how, *Geochem. Geophys. Geosyst.*, *10*, Q10014, doi:10.1029/2009GC002540.

Copley, A., J. P. Avouac, and J. Y. Royer (2010), India-Asia collision and the Cenozoic slowdown of the Indian plate: Implications for the forces driving plate motions, *J. Geophys. Res.*, *115*, B03410, doi:10.1029/2009JB006634.

Corrie, S. L., and M. J. Kohn (2011), Metamorphic history of the central Himalaya, Annapurna region, Nepal, and implications for tectonic models, *Geol. Soc. Am. Bull.*, *123*(9–10), 1863–1879.

Cottle, J. M., M. P. Searle, M. S. Horstwood, and D. J. Waters (2009), Timing of midcrustal metamorphism, melting, and deformation in the Mount Everest region of southern Tibet revealed by U (−Th)-Pb geochronology, *J. Geol.*, *117*(6), 643–664.

Coutand, I., D. M. Whipp, D. Grujic, M. Bernet, M. G. Fellin, B. Bookhagen, K. R. Landry, S. K. Ghalley, and C. Duncan (2014), Geometry and kinematics of the Main Himalayan Thrust and Neogene crustal exhumation in the Bhutanese Himalaya derived from inversion of multithermochronologic data, *J. Geophys. Res. Solid Earth*, *119*, 1446–1481, doi:10.1002/2013JB010891.

Daniel, C. G., L. S. Hollister, R. R. Parrish, and D. Grujic (2003), Exhumation of uthe Main Central Thrust from lower crustal depths, Eastern Bhutan Himalaya, *J. Metamorph. Geol.*, *21*(4), 317–334.

Dasgupta, S., J. Ganguly, and S. Neogi (2004), Inverted metamorphic sequence in the Sikkim Himalayas: Crystallization history, P-T gradient and implications, *J. Metamorph. Geol.*, *22*(5), 395–412, doi:10.1111/j.1525-1314.2004.00522.x.

Dasgupta, S., S. Chakraborty, and S. Neogi (2009), Petrology of an inverted Barrovian sequence of metapelites in Sikkim Himalaya, India: Constraints on the tectonics of inversion, *Am. J. Sci.*, *309*(1), 43–84, doi:10.2475/01.2009.02.

Foster, G., P. Kinny, D. Vance, C. Prince, and N. Harris (2000), The significance of monazite U–Th–Pb age data in metamorphic assemblages: A combined study of monazite and garnet chronometry, *Earth Planet. Sci. Lett.*, *181*, 327–340.

Foster, G., H. Gibson, R. Parrish, M. Horstwood, J. Fraser, and A. Tindle (2002), Textural, chemical and isotopic insights into the nature and behaviour of metamorphic monazite, *Chem. Geol.*, *191*, 183–207.

Foster, G., R. R. Parrish, M. S. Horstwood, S. Chenery, J. Pyle, and H. Gibson (2004), The generation of prograde P–T–t points and paths: A textural, compositional, and chronological study of metamorphic monazite, *Earth Planet. Sci. Lett.*, *228*, 125–142.

Gaidies, F., A. Petley-Ragan, S. Chakraborty, S. Dasgupta, and P. Jones (2015), Constraining the conditions of Barrovian metamorphism in Sikkim, India: P - T - t paths of garnet crystallization in the Lesser Himalayan Belt, *J. Metamorph. Geol.*, *33*, 23–44.

Gasser, D., E. Bruand, D. Rubatto, and K. Stüwe (2012), The behaviour of monazite from greenschist facies phyllites to anatectic gneisses: An example from the Chugach Metamorphic Complex, southern Alaska, *Lithos*, *134*, 108–122.

Goswami, S. (2005), *Inverted Metamorphism in the Sikkim-Darjeeling Himalaya: Structural, Metamorphic and Numerical Studies*, Univ. of Cambridge, Cambridge, U. K.

Harrison, T. M., F. J. Ryerson, P. LeFort, A. Yin, O. M. Lovera, and E. J. Catlos (1997), A late Miocene-Pliocene origin for the Central Himalayan inverted metamorphism, *Earth Planet. Sci. Lett.*, *146*(1–2), E1–E7.

Harrison, T. M., M. Grove, O. M. Lovera, and E. J. Catlos (1998), A model for the origin of Himalayan anatexis and inverted metamorphism, *J. Geophys. Res.*, *103*(B11), 27,017–27,032, doi:10.1029/98JB02468.

Henry, D. J., C. V. Guidotti, and J. A. Thomson (2005), The Ti-saturation surface for low-to-medium pressure metapelitic biotites: Implications for geothermometry and Ti-substitution mechanisms, *Am. Mineral.*, *90*(2–3), 316–328.

Henry, P., X. Le Pichon, and B. Goffe (1997), Kinematic, thermal and petrological model of the Himalayas: Constraints related to metamorphism within the underthrust Indian crust and topographic elevation, *Tectonophysics*, *273*(1–2), 31–56.

Herman, F., et al. (2010), Exhumation, crustal deformation, and thermal structure of the Nepal Himalaya derived from the inversion of thermochronological and thermobarometric data and modeling of the topography, *J. Geophys. Res.*, *115*, B06407, doi:10.1029/2008JB006126.

Hermann, J., and D. Rubatto (2003), Relating zircon and monazite domains to garnet growth zones: Age and duration of granulite facies metamorphism in the Val Malenco lower crust, *J. Metamorph. Geol.*, *21*(9), 833–852.

Hirschmiller, J., D. Grujic, B. Bookhagen, I. Coutand, P. Huyghe, J.-L. Mugnier, and T. Ojha (2014), What controls the growth of the Himalayan foreland fold-and-thrust belt?, *Geology*, *42*(3), 247–250, doi:10.1130/G35057.1.

Hoisch, T. D., M. L. Wells, and M. Grove (2008), Age trends in garnet-hosted monazite inclusions from upper amphibolite facies schist in the northern Grouse Creek Mountains, Utah, *Geochim. Cosmochim. Acta*, *72*, 5505–5520.

Holdaway, M. J. (2000), Application of new experimental and garnet Margules data to the garnet-biotite geothermometer, *Am. Mineral.*, *85*(7–8), 881–892.

Holland, T., and R. Powell (2011), An improved and extended internally consistent thermodynamic dataset for phases of petrological interest, involving a new equation of state for solids, *J. Metamorph. Geol.*, *29*(3), 333–383.

Huerta, A. D., L. H. Royden, and K. V. Hodges (1998), The thermal structure of collisional orogens as a response to accretion, erosion, and radiogenic heating, *J. Geophys. Res.*, *103*(B7), 15,287–15,302, doi:10.1029/98JB00593.

Huerta, A. D., L. H. Royden, and K. V. Hodges (1999), The effects of accretion, erosion and radiogenic heat on the metamorphic evolution of collisional orogens, *J. Metamorph. Geol.*, *17*, 349–366.

Iaffaldano, G., T. Bodin, and M. Sambridge (2013), Slow-downs and speed-ups of India–Eurasia convergence since ~20 Ma: Data-noise, uncertainties and dynamic implications, *Earth Planet. Sci. Lett.*, *367*, 146–156, doi:10.1016/j.epsl.2013.02.014.

Jaffey, A. H., K. F. Flynn, L. E. Glendenin, W. C. Bentley, and A. M. Essling (1971), Precision measurement of half-lives and specific of ^{235}U and ^{238}U, *Phys. Rev.*, *C4*, 1889–1906.

Janots, E., F. Negro, F. Brunet, B. Goffé, M. Engi, and M. L. Bouybaouène (2006), Evolution of the REE mineralogy in HP–LT metapelites of the Sebtide complex, Rif, Morocco: Monazite stability and geochronology, *Lithos*, *87*(3), 214–234.

Janots, E., F. Brunet, B. Goffé, C. Poinssot, M. Burchard, and L. Cemič (2007), Thermochemistry of monazite-(La) and dissakisite-(La): Implications for monazite and allanite stability in metapelites, *Contrib. Mineral. Petrol.*, *154*, 1–14.

Janots, E., M. Engi, A. Berger, J. Allaz, J. O. Schwarz, and C. Spandler (2008), Prograde metamorphic sequence of REE minerals in pelitic rocks of the Central Alps: Implications for allanite–monazite–xenotime phase relations from 250 to 610 C, *J. Metamorph. Geol.*, *26*(5), 509–526.

Janots, E., M. Engi, D. Rubatto, A. Berger, C. Gregory, and M. Rahn (2009), Metamorphic rates in collisional orogeny from in situ allanite and monazite dating, *Geology*, *37*(1), 11–14.

Jessup, M. J., D. L. Newell, J. M. Cottle, A. L. Berger, and J. A. Spotila (2008), Orogen-parallel extension and exhumation enhanced by denudation in the trans-Himalayan Arun River gorge, Ama Drime Massif, Tibet-Nepal, *Geology*, *36*(7), 587–590.

Kingsbury, J. A., C. F. Miller, J. L. Wooden, and T. M. Harrison (1993), Monazite paragenesis and U-Pb systematics in rocks of the eastern Mojave Desert, California, USA: Implications for thermochronometry, *Chem. Geol.*, *110*, 147–167.

Kohn, M. J., E. J. Catlos, F. J. Ryerson, and T. M. Harrison (2001), Pressure-temperature-time path discontinuity in the Main Central thrust zone, central Nepal, *Geology*, *29*(7), 571–574.

Kohn, M. J., M. S. Wieland, C. D. Parkinson, and B. N. Upreti (2004), Miocene faulting at plate tectonic velocity in the Himalaya of central Nepal, *Earth Planet. Sci. Lett.*, *228*(3), 299–310.

Kylander-Clark, A. R. C., B. R. Hacker, and J. M. Cottle (2013), Laser-ablation split-stream ICP petrochronology, *Chem. Geol.*, *345*, 99–112.

Larson, K. M., R. Bürgmann, R. Bilham, and J. T. Freymueller (1999), Kinematics of the India-Eurasia collision zone from GPS measurements, *J. Geophys. Res.*, *104*(B1), 1077–1093, doi:10.1029/1998JB900043.

Larson, K. P., F. Gervais, and D. A. Kellett (2013), A P–T–t–D discontinuity in east-central Nepal: Implications for the evolution of the Himalayan mid-crust, *Lithos*, *179*, 275–292.

Lavé, J., and J. P. Avouac (2000), Active folding of fluvial terraces across the Siwaliks Hills, Himalayas of central Nepal, *J. Geophys. Res.*, *105*(B3), 5735–5770.

Lavé, J., and J. P. Avouac (2001), Fluvial incision and tectonic uplift across the Himalayas of central Nepal, *J. Geophys. Res.*, *106*(B11), 26,561–26,591, doi:10.1029/2001JB000359.

Long, S., N. McQuarrie, T. Tobgay, and D. Grujic (2011), Geometry and crustal shortening of the Himalayan fold-thrust belt, eastern and central Bhutan, *Geol. Soc. Am. Bull.*, *123*(7–8), 1427–1447, doi:10.1130/b30203.1.

Ludwig, K. R. (2003), *A Geochronological Toolkit for Microsoft Excel*, Spec. Publ., vol. 4, 71 pp., Berkeley Geochronology Center, Berkeley, Calif.
McDonough, W. F., and S.-S. Sun (1995), The composition of the Earth, *Chem. Geol.*, *120*(3), 223–253.
McQuarrie, N., T. Tobgay, S. P. Long, P. W. Reiners, and M. A. Cosca (2014), Variable exhumation rates and variable displacement rates: Documenting recent slowing of Himalayan shortening in western Bhutan, *Earth Planet. Sci. Lett.*, *386*, 161–174.
Min, K., R. Mundil, P. R. Renne, and K. R. Ludwig (2000), A test for systematic errors in $^{40}Ar/^{39}Ar$ geochronology through comparison with U/Pb analysis of a 1.1-Ga rhyolite, *Geochim. Cosmochim. Acta*, *64*(1), 73–98.
Mitra, G., K. Bhattacharyya, and M. Mukul (2010), The Lesser Himalayan Duplex in Sikkim: Implications for variations in Himalayan shortening, *J. Geol. Soc. India*, *75*(1), 289–301.
Molnar, P., and J. M. Stock (2009), Slowing of India's convergence with Eurasia since 20 Ma and its implications for Tibetan mantle dynamics, *Tectonics*, *28*, TC3001, doi:10.1029/2008TC002271.
Mottram, C. M., T. Argles, R. Parrish, N. Harris, M. Horstwood, and S. Gupta (2014a), Tectonic interleaving along the Main Central Thrust, Sikkim Himalaya, *J. Geol. Soc.*, *171*, 255–268.
Mottram, C. M., C. J. Warren, D. Regis, N. M. Roberts, N. B. Harris, T. W. Argles, and R. R. Parrish (2014b), Developing an inverted Barrovian sequence: Insights from monazite petrochronology, *Earth Planet. Sci. Lett.*, *403*, 418–431.
Pyle, J. M., and F. S. Spear (2003), Four generations of accessory-phase growth in low-pressure migmatites from SW New Hampshire, *Am. Mineral.*, *88*, 338–351.
Renne, P. R., R. Mundil, G. Balco, K. Min, and K. R. Ludwig (2010), Joint determination of ^{40}K decay constants and $^{40}Ar^*/^{40}K$ for the Fish Canyon sanidine standard, and improved accuracy for $^{40}Ar/^{39}Ar$ geochronology, *Geochim. Cosmochim. Acta*, *74*(18), 5349.
Robinson, D. M., and N. McQuarrie (2012), Pulsed deformation and variable slip rates within the central Himalayan thrust belt, *Lithosphere*, *4*(5), 449–464.
Robinson, D. M., and O. Pearson (2013), Was Himalayan normal faulting triggered by initiation of the Ramgarh–Munsiari thrust and development of the Lesser Himalayan duplex?, *Int. J. Earth Sci.*, *102*, 1773–1790.
Rubatto, D., J. Hermann, and I. S. Buick (2006), Temperature and bulk composition control on the growth of monazite and zircon during low-pressure anatexis (Mount Stafford, central Australia), *J. Petrol.*, *47*(10), 1973–1996.
Schneider, C. A., W. S. Rasband, and K. W. Eliceiri (2012), NIH Image to ImageJ: 25 years of image analysis, *Nat. Methods*, *9*(7), 671–675.
Smith, H. A., and B. Barreiro (1990), Monazite U-Pb dating of staurolite grade metamorphism in pelitic schists, *Contrib. Mineral. Petrol.*, *105*, 602–615.
Spear, F. S. (2010), Monazite–allanite phase relations in metapelites, *Chem. Geol.*, *279*, 55–62.
Stacey, J. S., and J. Kramers (1975), Approximation of terrestrial lead isotope evolution by a two-stage model, *Earth Planet. Sci. Lett.*, *26*(2), 207–221.
Tobgay, T., S. Long, N. McQuarrie, M. N. Ducea, and G. Gehrels (2010), Using isotopic and chronologic data to fingerprint strata: Challenges and benefits of variable sources to tectonic interpretations, the Paro Formation, Bhutan Himalaya, *Tectonics*, *29*, TC6023, doi:10.1029/2009TC002637.
Tobgay, T., N. McQuarrie, S. Long, M. J. Kohn, and S. L. Corrie (2012), The age and rate of displacement along the Main Central Thrust in the western Bhutan Himalaya, *Earth Planet. Sci. Lett.*, *319-320*, 146–158.
Tomkins, H., R. Powell, and D. Ellis (2007), The pressure dependence of the zirconium-in-rutile thermometer, *J. Metamorph. Geol.*, *25*(6), 703–713.
van Hinsbergen, D. J., B. Steinberger, P. V. Doubrovine, and R. Gassmöller (2011), Acceleration and deceleration of India-Asia convergence since the Cretaceous: Roles of mantle plumes and continental Jaffey etcollision, *J. Geophys. Res.*, *116*, B06101, doi:10.1029/2010JB008051.
Warren, C. J., A. K. Singh, N. M. W. Roberts, D. Regis, A. M. Halton, and R. B. Singh (2014), Timing and conditions of peak metamorphism and cooling across the Zimithang Thrust, Arunachal Pradesh, India, *Lithos*, *200–201*, 94–110, doi:10.1016/j.lithos.2014.04.005.
Whipp, D. M., T. A. Ehlers, A. E. Blythe, K. W. Huntington, K. V. Hodges, and D. W. Burbank (2007), Plio-Quaternary exhumation history of the central Nepalese Himalaya: 2. Thermokinematic and thermochronometer age prediction model, *Tectonics*, *26*, TC3003, doi:10.1029/2006TC001991.
Wing, B. A., J. M. Ferry, and T. M. Harrison (2003), Prograde destruction and formation of monazite and allanite during contact and regional metamorphism of pelites: Petrology and geochronology, *Contrib. Mineral. Petrol.*, *145*, 228–250.